

The Hydrogen-Poor Superluminous Supernovae from the Zwicky Transient Facility Phase-I Survey: I. Data

Z. H. CHEN,¹ LIN YAN,² T. KANGAS,³ R. LUNNAN,⁴ S. SCHULZE,⁵ J. SOLLERMAN,⁴ D. A. PERLEY,⁶ T.-W. CHEN,⁴
A. GAL-YAM,⁷ X. F. WANG,^{1,8} I. ANDREONI,⁹ E. BELLM,¹⁰ J. S. BLOOM,^{11,12} K. BURDGE,¹³ A. BURGOS,¹⁴ D. COOK,¹⁵
A. DAHIWALE,¹³ K. DE,⁹ R. DEKANY,² A. DUGAS,¹⁶ S. FREDERIK,¹⁷ C. FREMLING,¹³ M. GRAHAM,⁹ M. HANKINS,¹⁸
A. HO,¹⁹ J. JENCSON,²⁰ V. KARAMBELKAR,⁹ M. KASLIWAL,¹³ S. KULKARNI,¹³ R. LAHER,¹⁵ B. RUSHOLME,¹⁵ Y. SHARMA,¹³
F. TADDIA,²¹ K. TAGGART,²² L. TARTAGLIA,²³ A. TZANIDAKIS,¹³ J. VAN ROESTEL,¹³ R. WALTER,⁹ Y. YANG,²⁴ Y. H. YAO,⁹
AND O. YARON⁷

¹Physics Department and Tsinghua Center for Astrophysics (THCA), Tsinghua University, Beijing, 100084, China

²Caltech Optical Observatories, California Institute of Technology, Pasadena, CA 91125, USA

³KTH Royal Institute of Technology, Stockholm, Sweden

⁴The Oskar Klein Centre, Department of Astronomy, Stockholm University, AlbaNova, SE-106 91 Stockholm, Sweden

⁵The Oskar Klein Centre, Department of Physics, Stockholm University, AlbaNova, SE-106 91 Stockholm, Sweden

⁶Astrophysics Research Institute, Liverpool John Moores University, 146 Brownlow Hill, Liverpool L3 5RF, UK

⁷Department of particle physics and astrophysics, Weizmann Institute of Science, 76100 Rehovot, Israel

⁸Beijing Planetarium, Beijing Academy of Sciences and Technology, Beijing, 100044, China

⁹Cahill Center for Astrophysics, California Institute of Technology, 1200 E. California Blvd. Pasadena, CA 91125, USA

¹⁰DIRAC Institute, Department of Astronomy, University of Washington, 3910 15th Avenue NE, Seattle, WA 98195, USA

¹¹Department of Astrophysics, University of California, Berkeley, CA 94720-3411, USA

¹²Lawrence Berkeley National Laboratory, 1 Cyclotron Road, MS 50B-4206, Berkeley, CA 94720, USA

¹³Division of Physics, Mathematics, and Astronomy, California Institute of Technology, Pasadena, CA 91125, USA

¹⁴Instituto de Astrofísica de Canarias, E-38 200 La Laguna, Tenerife, Spain

¹⁵IPAC, California Institute of Technology, 1200 E. California Blvd, Pasadena, CA 91125, USA

¹⁶Department of Physics and Astronomy, Watanabe 416, 2505 Correa Road, Honolulu, HI 96822, USA

¹⁷Department of Astronomy, University of Maryland, MD 20742-2421, USA

¹⁸Arkansas Tech University, Russellville, AR 72801, USA

¹⁹Department of Astronomy and Miller Institute for Basic Research in Science, University of California, Berkeley, CA, USA

²⁰Steward Observatory, University of Arizona, 933 North Cherry Avenue, Tucson, AZ 85721-0065, USA

²¹Department of Physics and Astronomy, Aarhus University, Ny Munkegade 120, DK-8000 Aarhus C, Denmark

²²Department of Astronomy and Astrophysics, University of California, Santa Cruz, CA 95064, USA

²³INAF-Osservatorio Astronomico di Padova, Vicolo dell'Osservatorio 5, I-35122 Padova, Italy

²⁴Department of Astronomy, University of California, Berkeley, CA 94720-3411, USA

Submitted to APJ

ABSTRACT

During the Zwicky Transient Facility (ZTF) Phase-I operation, 78 hydrogen-poor superluminous supernovae (SLSNe-I) were discovered in less than three years, making up the largest sample from a single survey. This paper (Paper I) presents the data, including the optical/ultraviolet light curves and classification spectra, while Paper II in this series will focus on the detailed analysis of the light curves and modeling. Our photometry is primarily taken by the ZTF in the g, r, i bands, and with additional data from other ground-based facilities and *Swift*. The events of our sample cover a redshift range of $z = 0.06 - 0.67$, with a median and 1σ error (16% and 84% percentiles) $z_{\text{med}} = 0.265^{+0.143}_{-0.135}$. The peak luminosity covers $-22.9 \text{ mag} \leq M_{g,\text{peak}} \leq -19.9 \text{ mag}$, with a median value of $-21.54^{+1.12}_{-0.61} \text{ mag}$. Their light curves evolve slowly with the mean rest-frame rise time of $t_{\text{rise}} = 42.0 \pm 17.8$ days. The luminosity and time scale distributions suggest that low luminosity SLSNe-I with peak luminosity $\sim -20 \text{ mag}$ or

extremely fast rising events ($< 10\text{--}15$ days) exist but are rare. We confirm previous findings that slowly rising SLSNe-I also tend to fade slowly. The rest-frame color and temperature evolution show large scatters, suggesting that the SLSN-I population may have diverse spectral energy distributions. The peak rest-frame color shows a moderate correlation with the peak absolute magnitude, *i.e.* brighter SLSNe-I tend to have bluer colors. With optical and ultraviolet photometry, we construct bolometric luminosity and derive a bolometric correction relation generally applicable for converting g, r -band photometry to bolometric luminosity for SLSNe-I.

Keywords: Stars: supernovae: general

1. INTRODUCTION

Superluminous supernovae (SLSNe) are a rare class of stellar explosions first discovered over fifteen years ago (*i.e.* SN 2005ap, Quimby et al. 2007). Their peak luminosities ($10^{43\text{--}44}$ erg s $^{-1}$) are 10 – 100 times higher than those of normal Type Ia and core-collapse supernovae (SNe). Their light curves (LCs) usually evolve rather slowly, with rise times of $\sim 20\text{--}100$ days. The combination of these two features can not be explained by conventional SN models, *i.e.* standard radioactive decay (Kasen 2017). With the discovery of the first several SLSNe (SN 2005ap, SN 2006gy, SN 2007bi & SN 2008es), it was quickly recognized that, like normal SNe, SLSNe can be divided into two spectroscopic subclasses, one with hydrogen emission lines (SLSNe-II, Miller et al. 2009; Gezari et al. 2009; Inserra et al. 2018b) and the other without hydrogen (H-poor, SLSNe-I, Quimby et al. 2007; Ofek et al. 2007; Gal-Yam et al. 2009; Smith et al. 2007; Gal-Yam 2012). In recent years, the subclass of H-poor but Helium-rich SLSNe (SLSNe-Ib) were first identified by Quimby et al. (2018), and later a sample by (Yan et al. 2020).

Three popular models have been proposed to explain the extraordinary radiative power of SLSNe. One involves energy injection from a central engine, such as the spin-down of a fast-rotating neutron star (magnetar) (Kasen & Bildsten 2010; Woosley 2010). Alternatively, the interaction between the SN ejecta and dense circumstellar material (CSM) can efficiently convert kinetic energy into radiation (Chevalier & Irwin 2011; Chatzopoulos et al. 2013). Finally, some SLSNe could be powered by massive amounts of ^{56}Ni synthesised in a pair-instability supernova explosion (PISN) of low-metallicity stars with masses $> 140 M_{\odot}$ (Woosley et al. 2007; Kasen et al. 2011). It is commonly accepted that most SLSNe-II are analogous to Type IIIn SNe (Schlegel 1990; Filippenko 1997), primarily powered by ejecta interactions with dense CSM (Ofek et al. 2007; Miller et al. 2010; Chevalier & Irwin 2011).

Between 2005 and 2009, a handful of SLSNe were discovered by several untargeted transient surveys which were not specifically targeting bright nearby galaxies.

This small number of luminous events sparked a flurry of studies in both theory and observation of SLSNe. The next big advance in this field came between 2009 and 2016 when large area, untargeted transient surveys started operating. For example, the Palomar Transient Factory (PTF; Law et al. 2009), the Pan-STARRS1 Medium Deep Survey (PS1 MDS; Chambers et al. 2016), the Catalina Real-time Transient Survey (CRTS; Drake et al. 2009), the All-Sky Automated Survey for Supernovae (ASAS-SN; Shappee 2014), the Dark Energy Survey (DES; The Dark Energy Survey Collaboration 2005) and Gaia Photometric Science Alerts (Gaia; Hodgkin et al. 2021) made major contributions to the discoveries of several dozen SLSNe at both low ($z \sim 0.2$) and high redshift ($z \sim 1$) (Nicholl et al. 2015; De Cia et al. 2018; Quimby et al. 2018; Lunnan et al. 2018; Angus et al. 2019). However, with over ~ 90 discovered SLSNe-I by the end of 2017, many questions regarding their physical nature still remained unclear. For example, the SLSN volumetric rates are poorly constrained, with only estimates from small SLSN-I samples (Quimby et al. 2013; McCrum et al. 2015; Prajs et al. 2017; Frohmaier et al. 2021). Attempts to examine the statistical distributions, such as luminosity functions, were also quite limited due to small number statistics.

Assembling a large sample of low- z SLSNe with a well-defined survey volume and cadence is one of the goals of the Zwicky Transient Facility (ZTF; Graham et al. 2019; Bellm et al. 2019a; Masci et al. 2019). ZTF utilizes an innovative, megapixel camera mounted on the Palomar Samuel Oschin 48 inch Schmidt telescope to reach a 47 deg^2 field of view (Dekany et al. 2020). ZTF can cover the full Northern Sky in 3 days down to a 5σ limiting magnitude of $20.5\text{--}20.8$ magnitude, which is about 3.5 and 0.5 magnitudes deeper than that of ASAS-SN (Shappee 2014), and the Asteroid Terrestrial-impact Last Alert System (ATLAS; Tonry et al. 2018), respectively. The ZTF survey offers several advantages for discovering rare transient events such as SLSNe. It is an untargeted, all sky, and moderately high cadence survey, probing large volumes with its large area coverage and deep sensitivity limits. Its well-defined survey

strategy – area coverage and cadence – also makes it possible to quantify the survey efficiency.

ZTF conducted several surveys with different cadences (ranging from minutes to days) and area coverage during the phase-I operation (Bellm et al. 2019b). Among them, a particularly important one for extragalactic transient studies is the Northern Sky Public Survey. ZTF covered roughly the entire northern sky accessible from Palomar, corresponding to a total sky area of $\sim 23,675 \text{ deg}^2$. In every 3 days, each field was observed once in g band and once in r band, with an interval of at least 30 minutes between observations.

Between March 17, 2018 and October 31, 2020, ZTF Phase-I¹ discovered and spectroscopically confirmed 85 SLSNe-I, 6 SLSNe-I.5 (classified as SLSNe-I but showing H lines after the peak) and 60 SLSNe-II (defined as SNe II with peak magnitudes brighter than -20.0 mag). The number of SLSNe discovered by ZTF from 2018 to 2020 (about 60 per year) is roughly 5 – 7 times higher than that detected in any previous year. The SLSN-I sample will be the focus of a series of three papers. Paper I (this paper) presents the observational data and analysis of the overall observational properties. Paper II (Chen et al. 2022) discusses the LC modeling and analysis of the LC morphology. Paper III (Yan et al. in preparation) will present the derived SLSN-I volumetric rates and luminosity functions at $z \leq 0.7$. Several additional papers based on some individual SLSNe discovered during the ZTF Phase-I operation have been recently published. Lunnan et al. (2020) showcased the first four SLSNe-I discovered by ZTF during its science commissioning phase. Yan et al. (2020) presented the discovery of six He-rich SLSNe-I (SLSNe-Ib), revealing additional constraints on the progenitor mass-loss history.

This paper is organized as follows. Section 2 introduces the selection and classification of this sample. Section 3 presents the photometry from ZTF and other facilities. Section 4 discusses our methodology with various photometric corrections and the calculations of peak absolute magnitudes. The measurements of time scales, colors, black-body temperatures and bolometric luminosities are presented in Section 5. Section 6 summarizes the conclusions. Throughout the paper, all magnitudes are in the AB system unless explicitly noted otherwise. We adopt a Λ CDM cosmology with

$H_0 = 67.7 \text{ km s}^{-1} \text{ Mpc}^{-1}$, $\Omega_M = 0.307$ and $\Omega_\Lambda = 0.693$ (Planck Collaboration et al. 2016).

2. THE SLSN-I SAMPLE FROM ZTF-I

During the phase-I survey, ZTF discovered 85 SLSNe-I. This paper focuses on 78 of these 85 events whose LCs have turned over from the peak by October 31, 2020, enabling better LC modeling. Of these 78 SLSNe-I, seven can be classified as He-rich SLSNe-Ib, including six published by Yan et al. (2020) and one by Terzner et al. (2020). For completeness, this sample paper also includes the four sources published in Lunnan et al. (2020). In addition, Schulze et al. (in preparation) will focus on an extremely slow and peculiar SLSN-I, ZTF18acenqto (SN2018ibb), and provided the derived parameters to include in our catalog.

Table A1 compiles the metadata for each of the targets, including the internal ZTF name, IAU name, right ascension (RA), declination (DEC), redshift, Galactic extinction $E(B - V)$, discovery group, and additional information on spectral classification. Our sample covers the redshift of $z \sim 0.06 - 0.67$ with a median and 1σ error (16% and 84% percentiles) $z_{\text{med}} = 0.265^{+0.143}_{-0.135}$. All redshifts in our sample are determined using the narrow emission lines from the host galaxy, except for seven events without host lines. The redshifts for these seven events are estimated from template matching by running *superfit* (Howell et al. 2006) over a range of z values. These redshifts are less accurate and marked with \star in Table A1. Figure 1 displays the redshift distribution of the full sample, including those derived from template fitting. To avoid possible biases caused by the choice of histogram grids, we apply kernel density estimation on all the histograms in this paper using a Gaussian kernel offered by the machine learning package Scikit-learn (Pedregosa et al. 2011), as shown in Figure 1.

2.1. Photometric Selection

Here we briefly describe the photometric selection system of our SLSN-I candidates. Daily ZTF alerts are ingested into a dynamic science portal called the GROWTH Marshal (Kasliwal et al. 2019). A filter is implemented within the Marshal to select SLSN candidates which are then visually examined and saved by human scanners. This filter adopts several cutoff conditions, including: [1] Not moving; the same alert is detected in two consecutive epochs with $\Delta t > 0.02 \text{ days}$. [2] Not a star, based on the SDSS star-galaxy scores (Tachibana & Miller 2018). [3] Excluding bogus alerts based on scores constructed by Duev et al. (2019). [4] Not in the galactic plane, with Galactic latitude $|b| > 7^\circ$. Using a scoring system, this candidate filter also gives preference

¹ The ZTF public survey transitioned to a 2-day cadence on October 1, 2020, however the official start of the ZTF Phase II is December 1, 2020. We picked our date range for the convenience of the sources analysed in our sample.

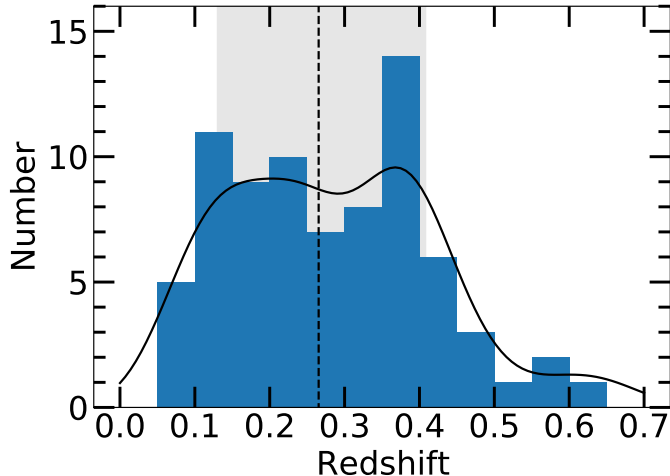


Figure 1. Distribution of redshifts for the sample of 78 SLSNe-I presented in this paper. The dashed line and the shaded area mark the median value and 1σ error (16% and 84% percentiles), $z_{med} = 0.265^{+0.143}_{-0.135}$. The black solid line shows the kernel density estimation of the distribution.

to slowly rising events with faint blue hosts. Additional considerations include spatial location (against nuclear transients), age (against old transients) and brightness of the candidates (against fainter ones).

With the above selection criteria, the possible candidates are finally saved during each scan session and get another round of vetting when spectral classification observations are planned. Any candidates brighter than 18.5 mag are classified by the ZTF Bright Transient Survey (BTS; Fremling et al. 2020). Their classification efficiency at ≤ 18.5 mag is very high, close to 95% (Fremling et al. 2020; Perley et al. 2020). Our classification is primarily focused on SLSN candidates fainter than 18.5 mag, mainly using the Spectral Energy Distribution Machine (SEDm; Blagorodnova et al. 2018) and the Double Beam Spectrograph (DBSP; Oke & Gunn 1983) mounted on the Palomar 60 inch (P60) and 200 inch (P200) telescope, respectively. Additional facilities include the Low Resolution Imaging Spectrometer (LRIS; Oke et al. 1995) on the Keck I telescope, the Alhambra Faint Object Spectrograph and Camera (ALFOSC) on the 2.56m Nordic Optical Telescope (NOT), SPectrograph for the Rapid Acquisition of Transients (SPRAT) on the 2m Liverpool Telescope (LT), and the Intermediate-dispersion Spectrograph and Imaging System (ISIS) on the 4.2m William Herschel Telescope (WHT). The SLSN project has at least 0.5 to 1 night of DBSP time on P200 per month for spectral classification (PI: Yan). More quantitative discussions on the completeness of spectral classification will be included in Paper III.

2.2. Spectral Classification

Every event in our sample has at least one spectrum and most have multi-epoch spectra. The hallmark spectral features for SLSNe-I are the five OII absorption features in the wavelength range of 3737 – 4650 Å in pre-peak and/or near-peak optical spectra. These were identified and discussed in Quimby et al. (2011, 2018). We utilize the large SLSN-I spectral template library assembled by Quimby et al. (2018), and update the library by adding the missing phase information to some of the templates. Our classification relies on matching with the spectral templates using SNID (Blondin & Tonry 2007) and *superfit*.

To determine the best matched spectral templates, we run both *superfit* and SNID on the smoothed spectra with host-galaxy emission lines removed and with redshifts fixed for most sources. If the spectrum of a SLSN-I has a good match with that of a SNIc but its *g*-band peak luminosity is higher than -20.0 mag, we classify this candidate as a SLSN-I since many SLSNe-I develop spectra similar to those of SNIc after the peak (Pastorello et al. 2010; Quimby et al. 2018; Gal-Yam 2019).

In Appendix A, Figures A7 – A9 present the best-fit spectral template for each event of our sample, with the information of event name, phase and template information labeled after the spectra. The phases are measured relative to the rest-frame *g*-band peak in this paper. We note that the phase differences between the observed spectra of our SLSNe-I and the templates in the library are not zero, but generally within 30 days (rest frame). This is not surprising since SLSNe-I can have similar photospheric spectra but different LC evolution time scales (see Kangas et al. 2017; Quimby et al. 2018).

The above classification procedure can sometimes give ambiguous results for a small number of events, *i.e.* two events for our sample. In these cases, we rely on additional LC information, such as rise time and peak luminosity to break the degeneracy. For example, ZTF19aacxrab and ZTF19aaqrime are almost equally well-matched with the spectral templates of SNIa and SLSN-I. In the case of ZTF19aacxrab, although the overall spectral features broadly match with those of SNIa, its spectrum lacks S II $\lambda\lambda$ 5433, 5606 commonly seen in SNIa. In addition, because of their slow rising LCs and high peak luminosities (*i.e.* ZTF19aaqrime has $M_g \sim -22.8$ mag), we adopt the SLSN-I classifications, corresponding to the template spectra of SN 2007bi and PTF09cnd, respectively.

In summary, the 78 sources listed in Table A1 can be classified as SLSNe-I according to their features of spectra and light curves. The classification spectra

are made available to the public as part of electronic data at the Journal website and will be uploaded to the Weizmann Interactive Supernova Data Repository (WiSeREP; Yaron & Gal-Yam 2012)².

3. OBSERVATIONS AND DATA

3.1. ZTF data and forced photometry

The bulk of the photometric data comes from ZTF, including the data from the public survey with a 3-day cadence, the ZTF partnership and Caltech surveys with a faster cadence (≤ 2 days) over smaller areas (Bellm et al. 2019b).

The IPAC ZTF pipeline produces reference-subtracted images using the ZOGY algorithm (Zackay et al. 2016) and aperture photometry for all transients detected at $\geq 5\sigma$. However, there are two issues with the LCs produced by this pipeline. One is that the reference images built in 2018 may contain signals from transients that exploded during the same period, for which the photometric offset needs to be corrected. The second issue is that the upper limits prior to the first detection are aperture photometry and based on the image noise measured over the entire quadrant. This can significantly underestimate transient signals.

To fix these two issues, we perform forced PSF photometry using the software provided by IPAC³. With a code from Yao et al. (2019), we refine the astrometric position of each event by using only the images around the peak phase. The very early and late-time forced photometry without transient signals allow us to compute baseline offsets to the LCs. In addition, we reject bad-quality data if $\text{infobit} \neq 0$, $\text{scisigpix} \geq 25$ or $\text{FWHM}(\text{seeing}) \geq 5''$, similar to what was used in Yao et al. (2019). The photometry of the same transient observed with different CCD quadrants can have a systematic offset. This problem gets fixed by our photometric reprocessing as well. For the final photometric collections, a detection is defined as 4σ above the background and an upper limit is computed at 3σ .

3.2. Supplemental photometry

3.2.1. LT and P60 photometry

When ZTF is not able to take observations due to scheduling conflicts or bad weather, or when the transient is fainter than the ZTF sensitivity limits, additional data will be taken with SEDM and the optical imager (IO:O) on the LT (Steele et al. 2004). The SEDM photometry is PSF fitted photometry and cal-

ibrated against either SDSS or PS1 reference images using the software Fpipe (Fremling et al. 2016). The LT photometric data are processed with a similar custom-built software (Taggart 2020).

3.2.2. Swift data

27 of 78 events in our sample have observations from the UV/Optical Telescope (UVOT; Roming et al. 2005) aboard the *Neil Gehrels Swift Observatory* (Gehrels et al. 2004). We retrieved the UVOT data from the NASA *Swift* Data Archive⁴, and used the standard UVOT data analysis software distributed with HEASoft version 6.19⁵, along with the standard calibration data. We manually define sky background apertures devoid of any sources. Four events in our sample, namely ZTF18aavrmcg, ZTF18acslpji, ZTF19aawfbtg and ZTF19abpbpt, have bright host galaxies. We therefore requested host-galaxy images at very late phases when the SNe had faded. The photometry for these four objects are obtained by subtracting out the host galaxy fluxes. For most of the other events, their host galaxies are very faint and contribute no more than 10% of the SN fluxes in the UV-bands, so no host-galaxy subtractions are applied.

All the photometry data are listed in Table A2, and are available to the public in electronic format at the journal website. The electronic tables contain the complete upper limits over much wider time ranges (early and late times) than what have been shown in the figures. For the visual display clarity, we show only a small number of photometric upper limits.

4. THE OBSERVED LIGHT CURVES

The observed LCs for the full sample are presented in Figures A1 - A6, where the left Y-axis is apparent magnitude and the X-axis is the rest-frame days relative to the g -band peak phase. For a small number of events without a g -band peak phase, we use the r -band peak phase as the reference. One striking feature apparent in Figures A1 - A6 is that a large fraction of the LCs in our sample show significant undulations, and some have multiple peaks. In Paper II, we find 34 – 62% of the well-sampled SLSNe-I have LC undulations. Among a small sub-set of SLSNe-I with early phase coverage, 6 – 44% show early double peak LCs. The quantitative analysis of the LCs and the discussions of these features are included in Paper II.

4.1. Extinction corrections and K -correction

² <https://www.wiserep.org/>

³ <http://web.ipac.caltech.edu/staff/fmasci/ztf/forcedphot.pdf>

⁴ <https://heasarc.gsfc.nasa.gov/cgi-bin/W3Browse/swift.pl>

⁵ <https://heasarc.nasa.gov/lheasoft/>

The Galactic reddening $E(B - V)$ is taken from the Schlafly & Finkbeiner (2011) dust map using the NASA/IPAC InfraRed Science Archive (IRSA) database. The extinction corrections at different wavelengths are computed using the empirical dust extinction laws of Fitzpatrick & Massa (2007) with $R_v = 3.1$.

Previous studies have shown that SLSN-I hosts are mostly low-mass, metal-poor dwarf galaxies (Lunnan et al. 2014, 2015; Leloudas et al. 2015; Perley et al. 2016; Angus et al. 2016; Chen et al. 2017a; Schulze et al. 2018). This is the case for most of the events in our sample. Because their LCs do not show particularly red colors at pre-peak phases, we do not make any host-galaxy reddening corrections to these events. However, a small fraction of SLSN-I hosts are massive ($10^{9-10} M_\odot$, Perley et al. 2016; Chen et al. 2017b), and the host-galaxy reddening in such cases can be large. We find that seven events in our sample (Table 1) have non-negligible host-galaxy reddening. They either reside in bright hosts ($M_r \lesssim -18.5$ mag) or have redder ($g - r$) colors at peak than average (see Figure 8), which is presumably due to host-galaxy reddening.

Table 1. Host-galaxy Reddening

Name	$E(B - V)_{\text{host}}$ (mag)	Method
ZTF18aajqcue	0.4 ^a	spec.temp
ZTF18acyxnyw	0.11	line ratio
ZTF19aaqrime	0.22	line ratio
ZTF19abcvwrz	0.07	spec.temp
ZTF19acvxquk	0.23	spec.temp
ZTF19acbonaa	0.18	line ratio
ZTF20abzaacf	0.24	spec.temp

^aEstimated in Lunnan et al. (2020).

The host-galaxy reddening is difficult to measure accurately, but can be roughly estimated using two different methods. The first one uses Balmer line ratio measured from the host-galaxy spectra. Without dust attenuation, the predicted line ratio between $H\alpha$ and $H\beta$ remains constant in a wide range of temperature and electron density in the nebular regions (*e.g.* $H\alpha/H\beta \approx 2.86$, Osterbrock & Ferland 2006). The attenuation caused by dust scattering is wavelength-dependent and stronger at shorter wavelengths. This method is affected by both stellar and supernova absorption features. We remove the stellar Balmer absorption using *FIREFLY* (Wilkinson et al. 2017) before we measure the line flux, but ignore the influence of supernova features. This method

is applied to the host spectra of ZTF18acyxnyw and ZTF19acbonaa. Note that the SN location may not coincide with the H II region responsible for the Balmer lines, so the real extinction at the SN site could be different from the inferred value. But such an estimation is at least an indicator of whether the galaxy has significant dust.

The second method is to infer the host-galaxy reddening by matching the observed spectrum (including spectral continuum slope and absorption features) with a SLSN-I template with negligible extinction and at a similar phase. For this method, the assumption is that the observed red spectral color is due to the host-galaxy reddening. The results from this method are very uncertain, but offer crude extinction estimates for those events without host emission lines. This method is applied to ZTF18aajqcue, ZTF19abcvwrz and ZTF19acvxquk. For example, to match the near-peak spectrum of ZTF18aajqcue, the $t \sim +54$ day template spectrum of SN 2007bi is required to be reddened by $E(B - V) \sim 0.4$ mag (Lunnan et al. 2020). Similarly, the +8 day spectrum of ZTF19acvxquk matches well with the -7 day template spectrum of PTF12gty after considering a host-galaxy reddening of $E(B - V) = 0.23$ mag. And the +13 day spectrum of ZTF19abcvwrz matches well with the +22 day template spectrum of PTF09cwl with $E(B - V) = 0.07$ mag (shown in Figures A7 – A9). Note that both PTF12gty and PTF09cwl have a faint, dwarf host, so their host-galaxy reddenings are assumed to be negligible (Quimby et al. 2018; Perley et al. 2016).

For ZTF19aaqrime and ZTF20abzaacf, we applied both of the above methods, since their spectra contain strong supernova signals and we are not able to remove the stellar absorption nor supernova features. The derived $E(B - V)$ for ZTF19aaqrime is 0.22 mag from the host-galaxy spectrum and 0.18 mag from template matching, which appear to be consistent. In the case of ZTF20abzaacf, the $E(B - V)$ derived from the spectral matching ranges from 0.22 – 0.26 mag, in contrast to the lower value (0.17 mag) inferred from the Balmer decrement. Its spectrum has very low signal-to-noise ratio at $H\beta$, and with both highly uncertain measurements, we adopt the average value of 0.24 mag from the template matching method.

One of the key parameters of SLSNe-I is the absolute g -band peak magnitudes. Proper estimate of this value requires proper K-corrections to derive reliable rest-frame values, either in g -band for sources at $z \leq 0.17$ or in r -band for sources at $z > 0.17$. This switch is chosen because the observed r -band LC at $z > 0.17$ is closer to the rest-frame g -band in wavelength.

Most events in our sample have at least one spectrum around the LC peak (*i.e.* $\lesssim 20$ days in rest frame), which allow us to compute the K-corrections using the formula described in Hogg et al. (2002). For those without spectra near the peak phases, we apply a constant K-correction of $-2.5 \times \log(1+z)$. This approximation is not too far from the spectral estimates, as shown below.

Figure 2 compares the calculated K-corrections based on observed spectra (blue dots) and an assumed 10^4 K blackbody spectral energy distribution (SED) (green line) with the constant correction (black line). The constant value of $-2.5 \times \log(1+z)$ appears to capture most of the corrections within a range of ± 0.1 mag (shaded region) for SLSNe-I at $0.06 < z < 0.67$. We list the K-corrections for each event in Table A3.

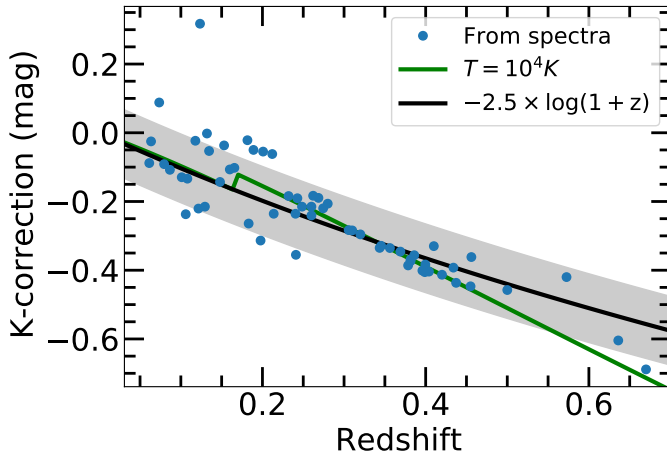


Figure 2. K-corrections from the observed band to the rest-frame g band for SLSNe-I around the peak. Blue points represent the corrections computed from the observed spectra. The black line shows the constant correction of $-2.5 \times \log(1+z)$ with an uncertainty of 0.1 mag shown by the gray shaded area. The green line shows the correction calculated assuming a blackbody spectrum with a temperature of 10^4 K. The break at $z = 0.17$ is caused by the change of observed band (from g to r band).

4.2. Empirical LC Fitting Method

The LC analysis requires estimates of various parameters such as peak magnitude, rise time and rise rate, which all involve numerical interpolation and fitting. We adopt a machine learning algorithm, Gaussian Process (GP) regression which has various kernel functions. The GP interpolation can reduce the influence of outliers and gives robust error estimates. We use a composite kernel which is the sum of Matérn kernel with a white noise kernel. We tested Matérn kernels with ν parameter of 3/2 (Matérn 3/2) (Inserra et al. 2018a; Angus et al. 2019; Lunnan et al. 2020) as well as $\nu = 5/2$ (Matérn 5/2).

When we compute peak magnitudes and phases, GP fit with Matérn 3/2 is performed in the flux space. The Python package `george` (Ambikasaran et al. 2016) and the Scikit-learn give comparable results.

4.3. LCs in Absolute g -band magnitudes

To set an approximate luminosity scale, we also plot the absolute magnitude on the right Y-axis of Figures A1 - A6. This is calculated by assuming a constant K-correction of $-2.5 \times \log(1+z)$. In these figures, the LCs have been corrected for the Galactic and host-galaxy reddening whenever possible.

To calculate the apparent peak magnitude and phase, we run the GP to interpolate the LCs in flux space. The errors are shown as 1σ uncertainty. The g -band absolute peak magnitudes are derived using $M_g = m_g - \mu - KC$, where μ is the distance modulus, KC is the K-correction, and m_g is the apparent g -band magnitudes corrected for both the host (in rest frame) and the Galactic extinction (in observed frame). The rest-frame g -band absolute peak magnitudes and the peak dates are tabulated in Table A3. The peaks of some events are not well constrained due to the poor sampling around the peak. Figure 3 shows the distribution of the g -band absolute peak magnitudes (M_g) for the ZTF sample, ranging from -19.9 to -22.9 mag with a median and 1σ error of $M_{g,med} = -21.54^{+1.12}_{-0.61}$ mag. Note that no selection bias (*e.g.* Malmquist bias) has been applied to the distribution shown in Figure 3.

5. LIGHT CURVE PARAMETERS

5.1. Rise/decay time scales – fast and slow SLSN-I events

Traditional rise times, defined as the interval between the explosion date and the peak, are notoriously difficult to measure, especially for distant transients such as SLSNe-I. Although the ZTF detection can go down to 20.5–21.0 magnitude, at the median redshift of our sample, it only probes an absolute magnitude of ~ -20 mag. The upper limits before the first detection usually can not place strong constraints on the LC evolution in very early phases and only about one-third of our sample have high-quality early time data. In addition, Anderson et al. (2018) shows that a SLSN-I (SN 2018bsz) can have a long, slowly rising “plateau” before a steeper, faster rise to the peak, which makes it harder to speculate explosion dates without enough deep, early data.

Instead of using the traditional rise time, we define $t_{rise/decay,x}$ as the time interval between the peak and the flux when it is at a fraction x of the peak value. Here the x factor can be 10% ($\Delta\text{mag} = 2.5$), or 1/2 ($\Delta\text{mag} \approx 0.75$). Time dilation is corrected for all time scale

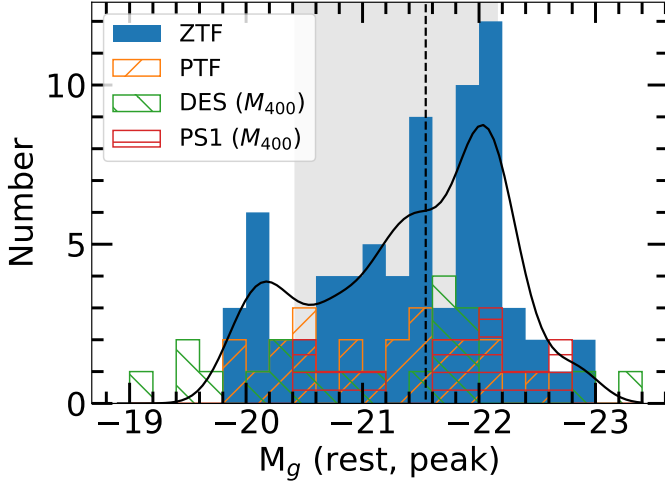


Figure 3. The distribution of the rest-frame g -band absolute peak magnitudes. The dashed line and shaded region mark the median value and the 1σ dispersion, $-21.54^{+1.12}_{-0.61}$ mag. The black solid line shows the kernel density estimation of the distribution. The SLSN-I samples from PTF (De Cia et al. 2018), DES (Angus et al. 2019) and PS1 (Lunnan et al. 2018) are plotted in different hatching patterns for comparison. DES and PS1 samples are measured at 400 nm, which is bluer than the g band (472 nm).

measurements. The derived $t_{\text{rise},10\%}$ and $t_{\text{rise/decay},1/2}$ are listed in Table A3. The poorly constrained time scales are not included in the following analysis.

Figure 4 shows a direct proportionality between $t_{\text{rise},1/2}$ and $t_{\text{rise},10\%}$ in the rest-frame g band. Linear fit gives $t_{\text{rise},1/2} = 0.70 t_{\text{rise},10\%} - 1.60$ days with 1σ uncertainty as small as ~ 3.1 days. The small scatter implies that the LC rise rates at the very early phases do not have significant differences in our sample. The rise times $t_{\text{rise},10\%}$ cover a wide distribution, ranging from 10 – 90 days, with the mean (median) value and a standard deviation of $\bar{t}_{\text{rise},10\%} = 42.0(38.7) \pm 17.8$ days.

Of the total 56 SLSNe-I with $t_{\text{rise},10\%}$ measurements, the two slowest rising events ZTF18acenqto (SN 2018ibb) and ZTF20aapaecd stand out in Figure 4, with time scales longer than $\bar{t}_{\text{rise},10\%} + 2\sigma = 78$ days. For ZTF20aadzbcf, although $t_{\text{rise},10\%}$ is not well constrained but its $t_{\text{rise},1/2}$ reaches 83 days, suggestive of an unusually long rise time. The fastest event in our sample is ZTF18aavrmcg (SN 2018bgv, Lunnan et al. 2020), which rises to the peak in less than 10 days. Such a fast and luminous event is very rare and it may be associated with the Fast Blue Optical Transients (FBOT, Drout et al. 2014; Ho et al. 2021).

Outside the $\pm 1\sigma$ range, we have 10 fast-evolving events with $t_{\text{rise},10\%} \leq \bar{t}_{\text{rise},10\%} - 1\sigma = 24$ days and 10 slow events with $t_{\text{rise},10\%} \geq \bar{t}_{\text{rise},10\%} + 1\sigma = 60$ days.

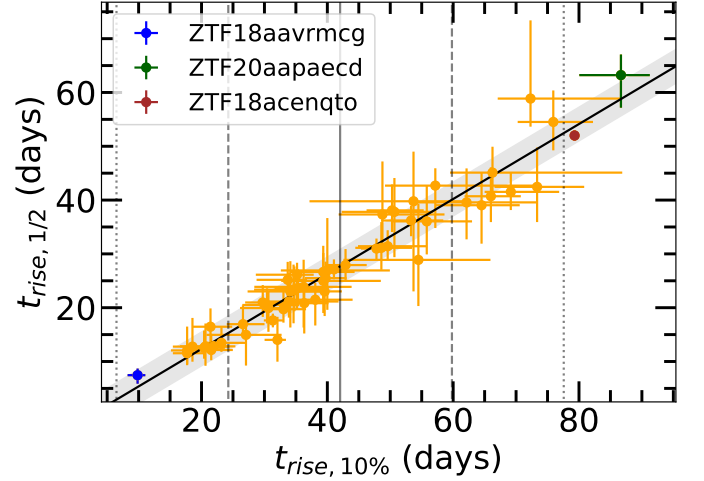


Figure 4. Rise time measured at 10% of the peak flux $t_{\text{rise},10\%}$ versus that measured at half of the peak flux $t_{\text{rise},1/2}$. The vertical solid grey line marks the mean value of $t_{\text{rise},10\%}$, the dashed and dotted lines represent the 1σ and 2σ uncertainties, respectively. The black solid line and shaded area show the linear fit to the measured time scales ($t_{\text{rise},10\%} = 0.70 t_{\text{rise},1/2} - 1.60$ days) and the 1σ dispersion. The events with extreme time scales are highlighted in different colors.

The $t_{\text{rise},10\%}$ shows a continuous distribution and can not be divided into two separate fast and slow subclasses, as indicated by previous studies (Nicholl et al. 2015; De Cia et al. 2018).

Figure 5 shows comparison of the rise and decay time scales measured at half of the peak flux for 54 events. Both rise/decay time scales show a distribution centered at ~ 25 days with an extended tail. For the whole sample, the rise and decay time scales show a positive correlation with a Spearman correlation coefficient of $\rho = 0.52$ and null probability $p < 10^{-4}$, *i.e.* slow-rising events tend to decay slow. Applying a linear fit, we find $t_{\text{decay},1/2} = (1.52 \pm 0.17) t_{\text{rise},1/2} - (5.72 \pm 4.68)$ days, which is similar to what was found in previous studies (Nicholl et al. 2015; De Cia et al. 2018). However, while most events follow this relation, seven events show significantly longer rise times than their decay times. As shown in Paper II, the fast, linear decline LCs are generally better characterized by CSM+Ni models where ejecta runs through CSM with either constant or wind-like density profiles. The magnetar models tend to have difficulties fitting steep, linear declines (for details, see Paper II).

It is interesting to note that four of the five SLSNe-Ib in the Yan et al. (2020) sample (ZTF18acyxnyw, ZTF19aawfbtg, ZTF19acgjpgh, ZTF20ablkuio) have rise time scales which are 9 – 32 days longer than that of the rise-decay time correlation. The last SLSN-Ib

(ZTF19aamhhiz) in the Yan et al. (2020) sample has a short rise time but much longer decay time. As noted in Yan et al. (2020), these SLSNe-Ib may have He-rich CSM and CSM interaction may affect the LC evolution before or after the peak. Detailed modeling and discussions of their LCs are given in Paper II.

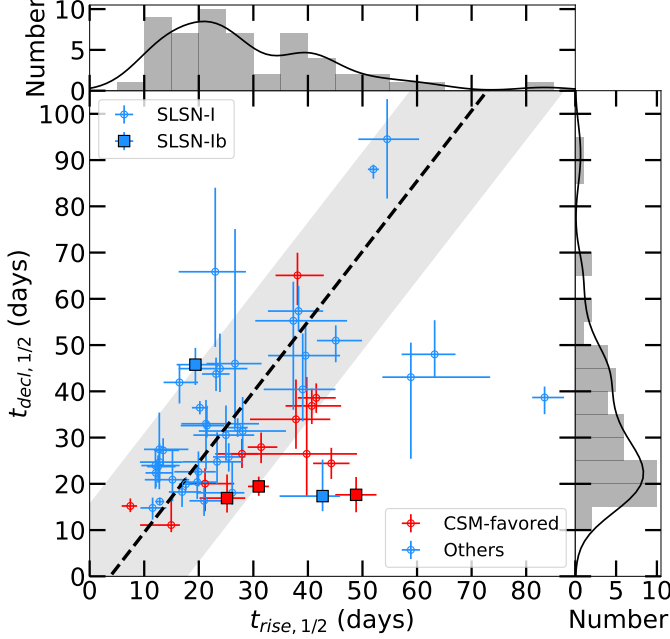


Figure 5. Time scales measured at half of the peak flux for the rising and declining portions of LCs. Circles represent normal SLSNe-I and squares represent He-rich SLSNe-Ib. The events with LCs favoring CSM+Ni model are highlighted in red (see LC modeling section in Paper II). The black dashed line and the shaded area show the best linear fit and 1-sigma error, $t_{\text{decay}} = 1.52 t_{\text{rise}} - 5.72$ days. The histograms along the horizontal and vertical axes show the distributions of the rise and decay time scales, respectively. The black solid lines show the kernel density estimation of the distributions.

Although SNeIc and SLSNe-I have similar post-peak spectra, they have very different peak luminosity and time scales. Figure 6 compares the peak M_g and rise times between normal SNeIc, broad-lined SNeIc (SNeIc-BL) and SLSNe-I. The SLSNe-I are from our sample, while the normal SNeIc sample and the SNeIc-BL sample are taken from Barbarino et al. (2021) and Taddia et al. (2019), respectively. We exclude two bright SNeIc from literature, iPTF12gtty and iPTF15eov, which can be better classified as SLSNe-I as suggested by their authors. Both SNeIc samples are obtained from the (intermediate) PTF, which has similar observation depth to ZTF. The overall distribution in Figure 6 is similar to that shown in De Cia et al. (2018). It should

be noted that correction for observational selection biases and volumetric correction are required to interpret the distribution correctly. The peak M_g of SLSNe-I is about 4 and 3 magnitude brighter than those of normal SNeIc and SNeIc-BL, respectively. All SLSNe-Ib have low luminosities and moderate rise times compared with normal SLSNe-I. SLSNe-I have significantly longer rise times and wider dispersion compared to those of SNeIc. First, this is physically related to the fact that they have larger ejecta masses and more massive progenitor stars (see Paper II). Second, SNeIc are primarily powered by radioactive decay which has a constant time scale of energy injection. In the magnetar model proposed for SLSNe-I, the time scale of energy injection depends on magnetic field B ($\propto B^{-2}$) and spin period P ($\propto P^2$). The LC width expands with the decrease of B (see Figure 2 of Kasen & Bildsten 2010). The large spread in their rise times could suggest that the magnetic field strengths of the neutron stars can vary over a wide range as well.

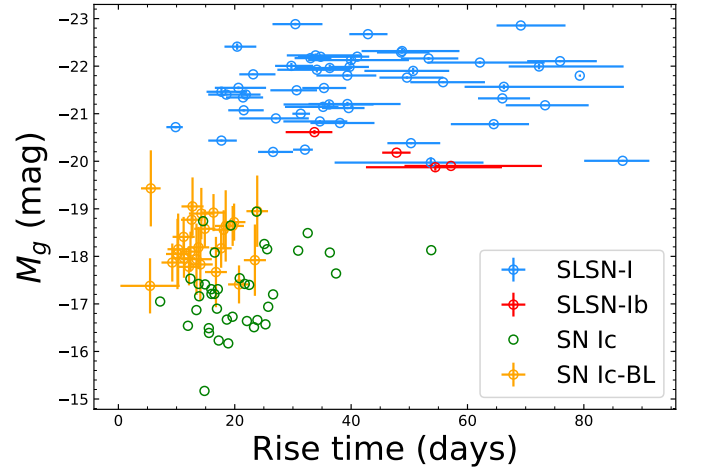


Figure 6. Rise times $t_{\text{rise},10\%}$ versus g -band absolute peak magnitudes M_g for SLSNe-I (this paper), normal SNeIc (from Barbarino et al. 2021) and broad-lined SNeIc (SNeIc-BL, from Taddia et al. 2019). The M_g of the SNeIc and SNeIc-BL samples is computed from the r -band magnitudes using a color correction of ~ 0.36 mag (Taddia et al. 2015; Prentice et al. 2016). The rise times of SNeIc and SNeIc-BL are measured from the explosion date in r band, which are slightly longer than $t_{\text{rise},10\%}$. The SLSNe-Ib in our sample are highlighted.

5.2. Color and blackbody temperature

Understanding the variation and uniformity of the SLSNe-I SEDs as a function of time should shed light on the physical nature of this population of stellar explosions. Although the complete characterization of the

SLSN-I SEDs is beyond the scope of this paper, we can infer some basic properties by examining the distributions of $(g-r)$ colors and blackbody temperatures since both parameters are determined by the transient SEDs.

Figure 7 shows the observed color evolution as a function of time. All of the colors have been corrected for reddening but not for K-corrections, since that requires better spectral coverage than we have. As expected, the overall $(g-r)$ color trend evolves from blue (*i.e.* ~ -0.3 mag, hotter temperatures) at early phases to red and reaches $(g-r) \sim +0.8$ mag at about 2 months after the peak. In our sample, four events have peculiar color (temperature) evolution, and do not follow the general trend. We discuss these outliers below. We further examine the distribution of the observed $(g-r)$ color obtained at the maximum light in Figure 8, which also shows a small number of SLSNe-I with red colors. At the peak phases, the median observed color is close to zero, $(g-r)_{med} = -0.03^{+0.15}_{-0.13}$ mag.

Figures 7 and 8 show large scatters. The observed colors are not easy to interpret because they sample different parts of the SEDs, depending on the transient redshifts. The proper measurements are the rest-frame color tracks, however, reliable results would require many more spectra than our sample has. Here we compute only the rest-frame $(g-r)$ colors at the peak phase using the color corrections computed from the near-peak spectra. The rest-frame $(g-r)$ colors are corrected from the observed $(g-r)$ for the events at $z \leq 0.17$ and $(i-r)$ for $z > 0.17$, if photometry data and spectra are available. All the peak colors are listed in Table A4. The green histogram in Figure 8 shows that the median rest-frame $(g-r)_{rest,med}$ is $-0.20^{+0.19}_{-0.10}$ mag, which is consistent with -0.27 mag calculated from the PTF SLSN-I sample (De Cia et al. 2018). The large scatter in the peak rest-frame $(g-r)$ indicates that the SEDs of SLSNe-I may show a diverse shape and hence a wide range of blackbody temperatures.

Figure 9 illustrates a moderate correlation ($\rho = 0.54$, $p < 10^{-3}$) between the peak rest-frame $(g-r)$ colors and the g -band absolute peak magnitudes $M_{g,peak}$, *i.e.* brighter SLSNe-I tend to have bluer color, which was also previously found by Inserra & Smartt (2014) and De Cia et al. (2018) in smaller samples. If combined with the PTF sample from De Cia et al. (2018), the correlation becomes stronger ($\rho = 0.55$, $p < 10^{-4}$), and can be described by a linear function, $M_{g,peak} = (8.3 \pm 1.6) \times (g-r) - (19.5 \pm 0.3)$ mag, with 1σ error of 1.3 mag. This correlation can be used in cosmological searches of SLSNe, *e.g.* Inserra et al. (2021). However, this is beyond the scope of this paper.

To fit the blackbody temperature, we adopt a modified blackbody function, defined by $f_\lambda = \max[0, 1 - A \times (1.0 - \lambda/3000.0)] \times B_\lambda$, with B_λ being the Planck function, and A being the scaling factor. The modified blackbody function aims to quantitatively capture the variations in the UV spectral suppression for different events, as shown by the HST UV spectra of SLSNe-I (Yan et al. 2017, 2018). The scaling factor A is derived from the fitting at $\lambda \leq 3000 \text{ \AA}$, set to zero at $\lambda \geq 3000 \text{ \AA}$ and fit in a range of 0–3. Larger scaling factors represent stronger suppression in UV and $A = 1$ represents the SED function used in Nicholl et al. (2017). The error associated with the temperature is estimated using the Markov Chain Monte Carlo (MCMC) method.

Of the 78 events in our sample, only 15 have at least 3 epochs of *Swift* UV photometry for properly computing the blackbody temperatures. In Figure 10, the left panel shows the temperature evolution tracks for 12 events, and the right panel shows the rest three with peculiar color/temperature evolution. Although the statistics is not large, Figure 10 indicates the large temperature spread at any given phase. In the left panel, some SLSNe-I have high temperatures at ~ 15000 K at $t \sim -15$ days, and cool down to ~ 9000 K at $+20$ days. Interestingly, there are also two cooler SLSNe-I with the peak temperatures less than ~ 10000 K. We perform a polynomial fit to the temperature tracks and derive $T = 0.092121 t^3 - 3.3591 t^2 - 190.28 t + 13358$ K and $T = -0.042888 t^3 + 0.4073 t^2 - 26.46 t + 8880$ K for the high and low temperature tracks, respectively. These are shown as blue and red shaded regions with the $\pm 1\sigma$ uncertainty in Figure 10. Consistent with the temperature evolution, the $(g-r)$ colors of low-temperature events are $\sim 0.2 - 0.3$ mag redder than those of high-temperature ones at the peak but become indistinguishable from that of the full sample after $+15$ days after the peak.

Moreover, the color distribution plots suggest that there are more low-temperature SLSNe-I. For instance, 10 out of 35 (29%) events are found to have redder peak rest-frame colors than the two low-temperature events (~ 0.10 mag). However these 10 events have no UV photometry available, thus no temperature measurements. It is possible that these 10 red events could also have low peak temperatures.

In summary, our measurements show that the SLSN-I population can have a wide range of temperatures (colors), from high (blue) to low (red). Although we have the temperature measurements for only two cool events, the color distribution plots suggest that there are more such events. We infer that the SEDs of SLSNe-I probably have diverse shapes and evolution tracks.

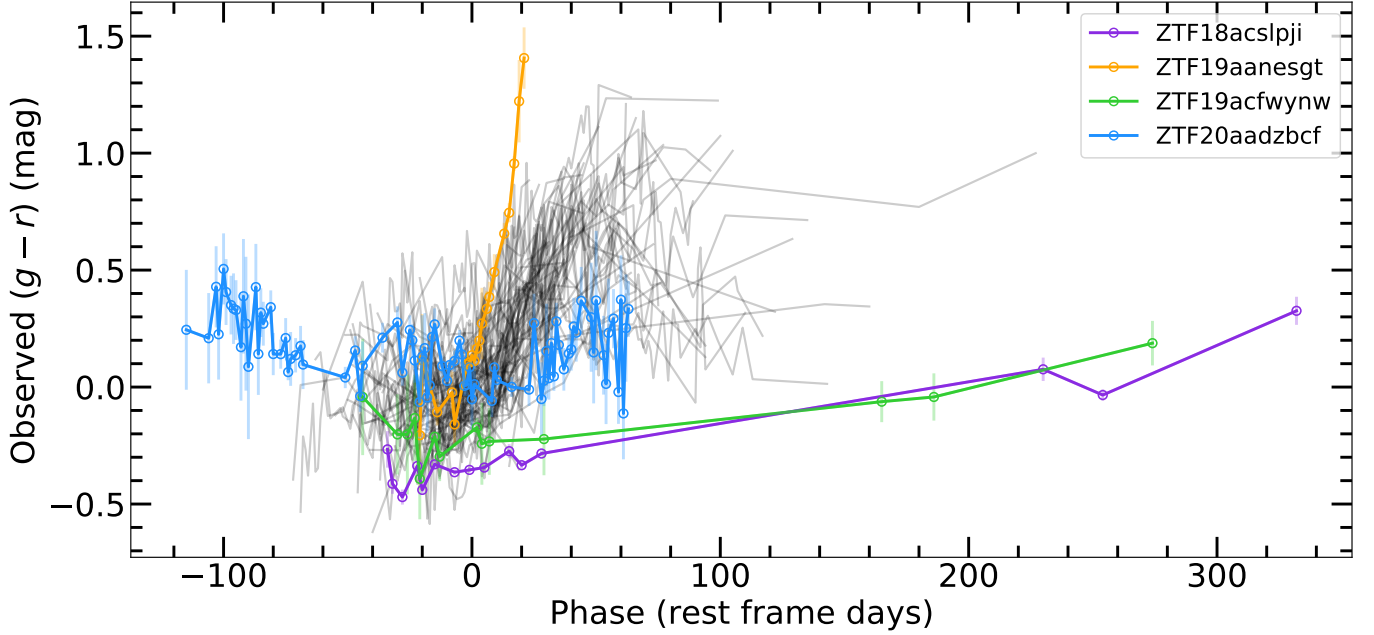


Figure 7. The observed $(g - r)$ color evolution tracks with time. We highlight four events whose $(g - r)$ color tracks do not follow the general trend shown in gray.

Finally, we discuss four peculiar events that have extraordinary color and temperature evolution as shown in Figures 7 and 10.

ZTF18acslpji (SN 2018hti) is well sampled in UV and shows notably higher temperatures and much bluer $(g - r)$ colors compared with other events. Its LC can be well reproduced by a magnetar model (Lin et al. 2020). This event may represent some of the population with higher temperatures and bluer SEDs. However, we caution that this event has a very high Galactic extinction $E(B - V) = 0.4$ mag. The dust extinction corrections in the UV-bands are highly uncertain. Finally, this event has quite blue $(g - r)$ colors at $> +100 - 200$ days. After visually examining its spectra, we conclude that the late time $(g - r)$ colors are strongly influenced by emerging SN emission features.

ZTF20aadzbcf has two almost equally bright LC peaks (at phase ~ -60 and 0 days, respectively) and the longest half-maxima rise time scale of 83.4 days (see the right-most point in Figure 5). Both its color and temperature evolutions are peculiar. The $(g - r)$ color around two peaks shows similar evolutionary trends, *i.e.* initially evolving from red to blue before the peak and then turning red after the peak. During the phase from -75 days to $+35$ days, its temperature remains almost constant of ~ 10000 K, which could be due to the absence of sampling. Such a long time scale and double-peak evolution are unexpected for a simple radiative cooling or magnetar model. Dessart (2019) examined the color evolution for various configurations of magne-

tar models, and found that almost all have fairly blue colors in the early phase and none shows the color change of ~ 0.7 mag from red to blue. The ejecta interaction with an extended H-poor CSM could be a possible explanation.

ZTF19aanesgt evolves into a very red event much faster and redder than other objects in our sample. No temperature evolution is computed due to the lack of UV data. This event is somewhat similar to ZTF18aavrmcg (SN 2018bgv), both belonging to the fast-evolving and CSM-model-favored events (see LC modeling in Paper II), though it has much redder $(g - r)$ color at $+20$ days after the peak. Such a red color and fast LC evolution could also be consistent with a magnetar model with high kinetic energy, as shown in Figure 13 of Dessart (2019). Nevertheless, the Fe II velocity and the kinetic energy of the ejecta derived for ZTF19aanesgt are $\sim 13800 \text{ km s}^{-1}$ and 4.03×10^{51} erg, respectively, which are only slightly higher than the average value (see Paper II). Thus other mechanisms may be needed to account for the peculiar properties of ZTF19aanesgt.

Finally, unlike any other SLSN-I, ZTF19acfwynw shows unusually high temperatures which are rising as the luminosity declines. At the early phases, its colors are blue, consistent with having high temperatures. Although the black-body temperatures at late time have large errors due to contamination of increasingly strong nebular emission lines, its spectral sequence has revealed a clear excess of UV continuum emission well past the peak phase. One possible explanation is CSM inter-

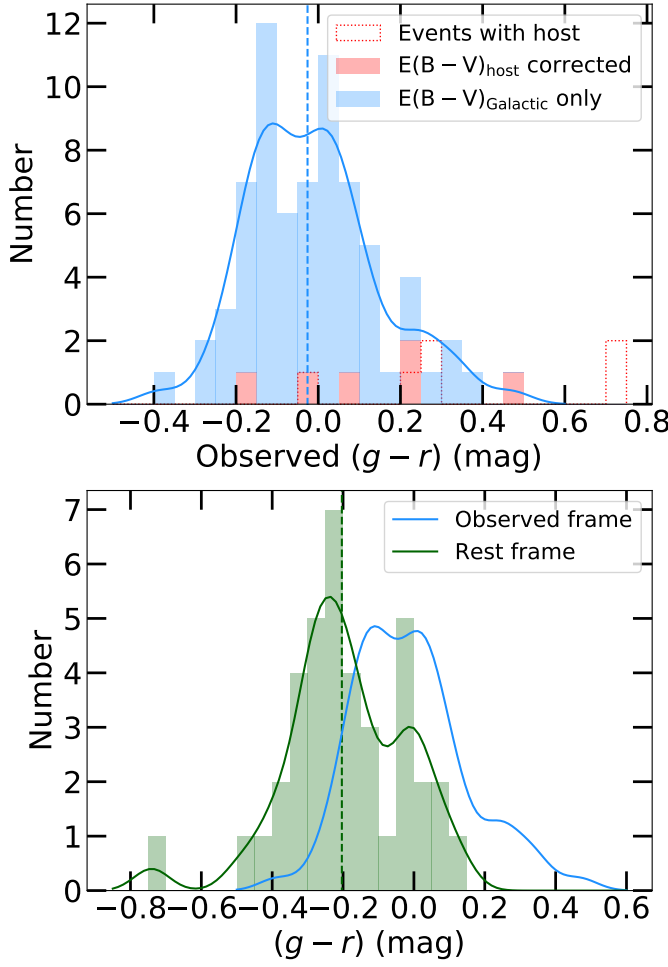


Figure 8. The distribution of the $(g-r)$ colors at peak. **Top panel:** The red dotted line represents the original colors of the events with host-galaxy reddening and the red area shows their corrected observed color. The blue area represents the observed colors of the events with only Galactic extinction correction. After host-galaxy reddening correction, the observed $(g-r)$ color at peak has a median value with the 1σ dispersion of $-0.03^{+0.15}_{-0.13}$ mag, marked by the blue dashed line. The blue solid line shows the kernel density estimation of the distribution. **Bottom panel:** The green area represents the rest-frame colors of the events with K-correction. The rest-frame $(g-r)$ color at peak has a median value with the 1σ dispersion of $-0.20^{+0.19}_{-0.10}$ mag, which is represented by the green dashed line. The green and blue solid lines show the kernel density estimations of the rest-frame colors and the observed colors (normalized to the number of the rest-frame colors), respectively.

action, which could offer an additional heating source, boosting the emission at shorter wavelength. The presence of [O III] lines in the nebular phase spectra indicates the ionization in local environment, which is consistent with the high temperature of this system. Another possibility is that the ejecta could be ionized by

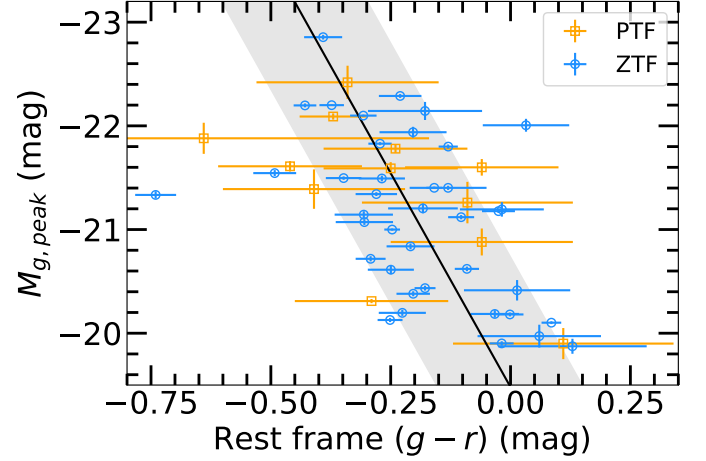


Figure 9. The correlation between the g -band absolute peak magnitudes $M_{g,peak}$ and the rest-frame $(g-r)$ colors. The linear fit and 1σ error are shown by the black line and the shaded area. The SLSN-I sample from this paper is marked in blue while that from PTF (De Cia et al. 2018) is in orange.

the ionizing flux from a long-lived central source (*e.g.* a magnetar, Margutti et al. 2017). Ionization can increase the optical opacity dominated by the electron scattering and decrease the UV opacity dominated by line transitions of metals, which leads to a shift of the peak of the SED from optical to UV frequencies.

It is worth noting that three out of the four events with peculiar color and temperature evolution are not well fit by simple magnetar models. It is likely CSM interaction plays significant roles in these three systems. Additional modeling and analysis are presented in Paper II.

5.3. Bolometric correction and bolometric LC

Bolometric light curve is an important indicator of the total radiative energy of a transient and sets constraints on the possible explosion mechanisms. Due to the high photospheric temperatures of SLSNe-I, UV radiation contributes to a large fraction of their emission (Yan et al. 2017, 2018). Since only a small portion of the sample has UV data, we need to first derive an empirical bolometric correction (BC) relation, which can tie g - and r -band photometry to the bolometric luminosity, with $\log L_{bol} = \log L_{gr} + BC$ ⁶. Here L_{gr} is the sum of the g - and r -band luminosities.

Lyman et al. (2013) derived bolometric corrections for a sample of core-collapse SNe at low redshifts using their well-observed SEDs. We adopt a similar method and

⁶ Another definition of bolometric correction is $M_{bolo} = M_K + BC_K$ for K -band absolute magnitude M_K , where M_{bolo} is bolometric magnitude. Our correction is applied to two bands (g and r), and we use the definition introduced in §5.3.

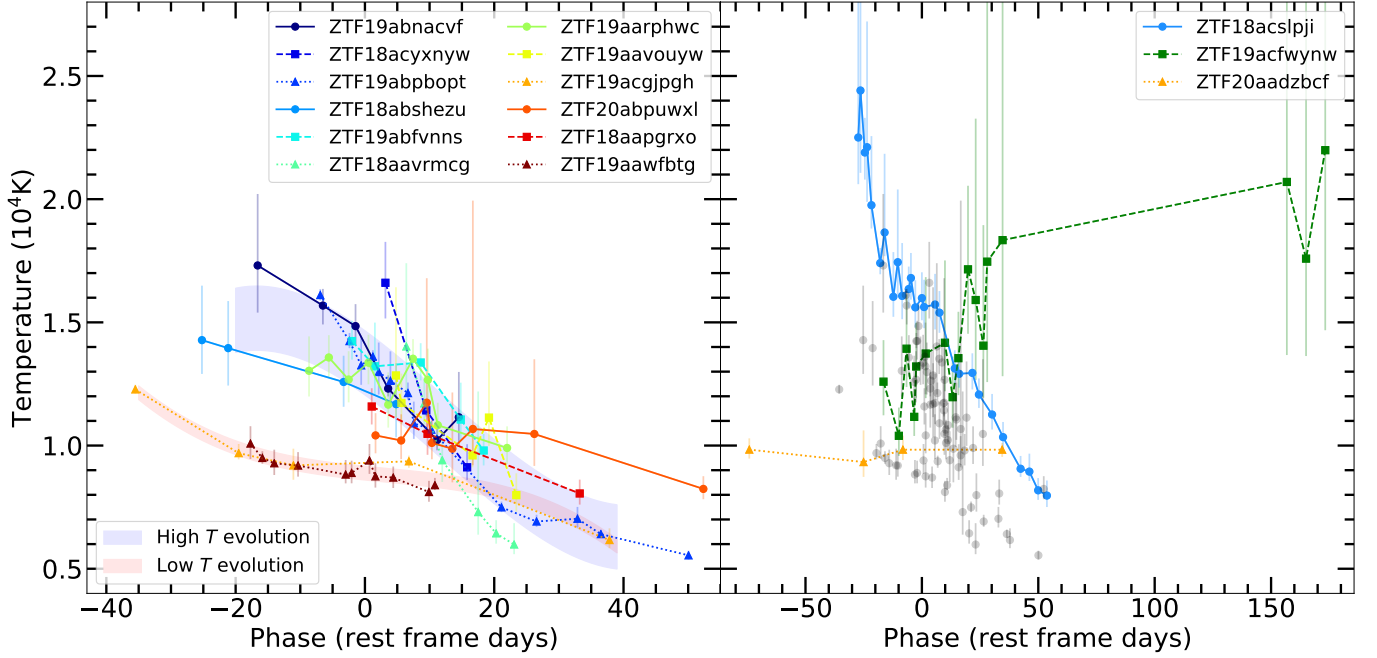


Figure 10. Blackbody temperature evolution as a function of time. **Left panel:** We include 12 of 15 events with at least 3 epochs of UV data. We apply third-order polynomial fits to the temperature evolution of two low-temperature events, ZTF19acgjpgh and ZTF19aawfbtg, and show the result with the 1σ error in the red shaded area. Similarly, the fit of 10 high-temperature events is shown by the blue shaded area. **Right panel:** We highlight the three extraordinary events and plot the 12 normal events in gray for comparison.

apply it to our sample. The basic concept is following. Bolometric correction is strongly influenced by the redshift and the temperature (slope of the spectra) at each epoch. As the observed $(g-r)$ color is also largely determined by the same two parameters, it is expected to see a correlation between the BC and the $(g-r)$ color. This correlation can serve as the basis of constructing bolometric LCs with only optical data.

We first compute the bolometric luminosity at the epochs when both UV and optical data are available, using the modified blackbody SED fit described in §5.2. The UV scaling factor A is derived by fitting the UV to optical SEDs. For the epochs without UV data, we set $A = 1.55$, which is the median value of the epochs with UV data. The bolometric luminosities are shown in Figure 12 (only 15 events with at least three-epoch UV photometry) and listed in Table A5.

Figure 11 shows the observed $(g-r)$ color versus the bolometric correction, *i.e.* $\log L_{\text{bolo}}/L_{\text{gr}}$, the luminosity ratio. We apply a third-order polynomial fit by optimizing a Gaussian likelihood function and derive an empirical relation as $\log(L_{\text{bolo}}/L_{\text{gr}}) = -1.040x^3 + 1.244x^2 - 0.269x + 0.411$, where $x = (g-r)$. Each point is weighted by the errors of both color and luminosity ratio. This equation can be used to compute the BC for low- z SLSNe-I with similar $(g-r)$ color evolution as our sample. Note that our fit is applicable for

$-0.4 < (g-r) < +0.9 \text{ mag}$, the phase range of $-74 \text{ days} < \text{phase} < +173 \text{ days}$ and $0.06 < z < 0.57$.

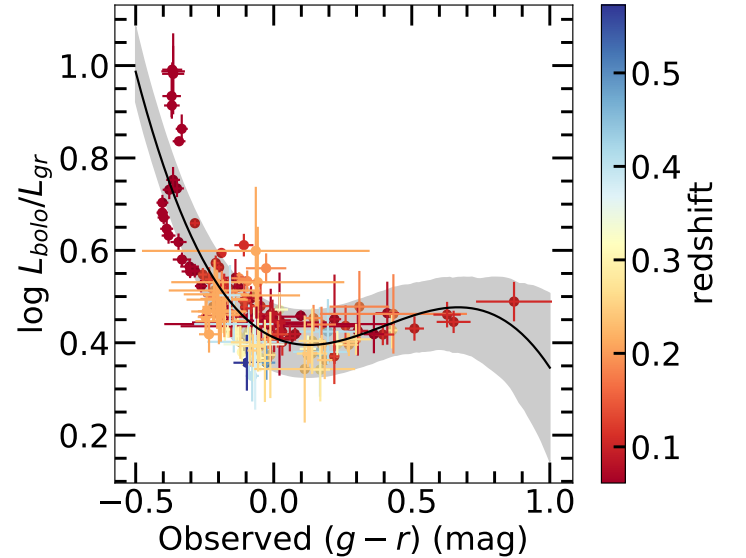


Figure 11. Bolometric corrections (ratio between bolometric luminosity and the gr -band luminosity) derived from the events with both UV and gr -band photometry. The color bar on the right indicates the redshift of each data point. The black solid line shows the result of third-polynomial fit and the gray area shows 1σ uncertainty.

As inferred from the residuals, the systematic error for the derived bolometric luminosity is about 18%. The BC uncertainty (shown as the shaded area in Figure 11) is the combined errors from MCMC estimates and the systematic error. This error is the dominant one compared with other error sources like host-galaxy reddening and redshifts. In Figure 12, the bolometric luminosities constructed with both UV and optical photometry are consistent with the ones derived from g - and r -band photometry. This illustrates the reliability of our method.

The bolometric LCs derived from g - and r -band photometry are shown in Figure 13. The errors of both color and bolometric correction are included. ZTF19aauiref and ZTF19acvxqk are excluded in this figure due to the bad photometry quality. Figure 13 illustrates a diversity in both peak luminosities and LC widths. Bumpy LCs are commonly seen and we perform detailed analysis in Paper II.

The peak bolometric luminosities are tabulated in Table A3 and the distribution is shown in Figure 14. The peak bolometric luminosities and the absolute peak magnitudes (Figure 3) have bimodal distributions. These are the raw distribution functions without any corrections for selection biases. Further studies are required to confirm such bimodal distributions. The peak bolometric luminosity spans from 3.28×10^{43} to $7.83 \times 10^{44} \text{ erg s}^{-1}$, with a median value and the 1σ dispersion of $L_{\text{bolo}, \text{med}} = 1.98^{+2.07}_{-1.42} \times 10^{44} \text{ erg s}^{-1}$. Compared to the median peak luminosity of SNe Ib/c ($\sim 2 \times 10^{42} \text{ erg s}^{-1}$, Prentice et al. 2016), SLSNe-I are about 100 times more luminous, indicating different energy sources and/or explosion mechanisms from normal cc-SNe.

6. CONCLUSIONS

The large sky coverage, high sensitivity and uniform cadence have made ZTF a very efficient discovery machine for superluminous supernovae. During the phase-I operation of ZTF survey, a total of 85 SLSNe-I were discovered. This paper presents 78 SLSNe-I whose LCs cover both pre- and post-peak phases. The other 7 SLSNe-I were still rising before October 30, 2021, and are not included in current analysis. This sample represents the largest sample of SLSNe-I at $z < 1$ discovered from a single survey. Our main findings are summarized as follows.

1. The rise times $t_{\text{rise}, 10\%}$ of our SLSN-I events have a mean value of 42.0 ± 17.8 days. SLSNe-I with $t_{\text{rise}, 10\%}$ shorter than 10 days are extremely rare, with only one event in our sample. Slow events with $t_{\text{rise}, 10\%} > 78$ days are also rare, only 3 (5%) in our sample. The $t_{\text{rise}, 10\%}$ shows a continu-

ous distribution and can not be divided into two clearly detached subclasses. The half-maxima rise and decay time scales show a positive correlation, *i.e.* slow-rising events tend to decay slow. We also find that the SLSNe-I with LCs favoring the CSM+Ni model tend to have longer rise times but shorter decay times compared with the SLSNe-I which can be well fit by the magnetar model. This is consistent with the explanation from Chatzopoulos et al. (2012) that CSM models fit better with steep, linear decline LCs. Compared with SNe Ic, SLSNe-I have significantly longer rise times and wider dispersion.

2. The observed $(g - r)$ color at peak has a median value of $-0.03^{+0.15}_{-0.13} \text{ mag}$ and the rest-frame $(g - r)$ color $-0.20^{+0.19}_{-0.10} \text{ mag}$. The majority of our SLSNe-I follows a wide color trend that evolves from blue ($(g - r) \sim -0.3 \text{ mag}$) at early phases to red, and reaches $(g - r) \sim +0.8 \text{ mag}$ at about 2 months after the peak. The peak rest-frame $(g - r)$ color is moderately correlated with the g -band absolute peak magnitudes, *i.e.* brighter SLSNe-I tend to have bluer color.
3. Most events in our sample follow a general temperature trend of relatively high and rapid evolution, while two show a low and slowly evolving trend.
4. We find four peculiar events that have extraordinary temperature and $(g - r)$ color evolution. ZTF18acslpji shows a notably high temperature and blue color. ZTF20aadzbcf remains almost at a constant temperature of 10000 K for over 100 days and has a double-peak color evolution like its LC. ZTF19acfwynw shows an unusual temperature evolution, which slowly rises from 13000 K at -20 day to 20000 K at $+170$ day. The color of ZTF19aanesgt turns red much faster than that of any other event.
5. The absolute peak magnitudes of our SLSN-I sample are $-22.9 \text{ mag} \leq M_g \leq -19.9 \text{ mag}$, with a median value and the 1σ error of $-21.54^{+1.12}_{-0.61} \text{ mag}$. On average, the peak M_g of SLSNe-I is around 4 mag and 3 mag brighter than normal SNe Ic and SNe Ic-BL, respectively. The peak bolometric luminosities of our sample distribute from 3.28×10^{43} to $7.83 \times 10^{44} \text{ erg s}^{-1}$ and have a median value with the 1σ dispersion of $1.98^{+2.07}_{-1.42} \times 10^{44} \text{ erg s}^{-1}$.
6. We derive a bolometric correction relation, $\log(L_{\text{bolo}}/L_{gr}) = -1.040x^3 + 1.244x^2 - 0.269x + 0.411$, where $x = (g - r)$. This equation allows

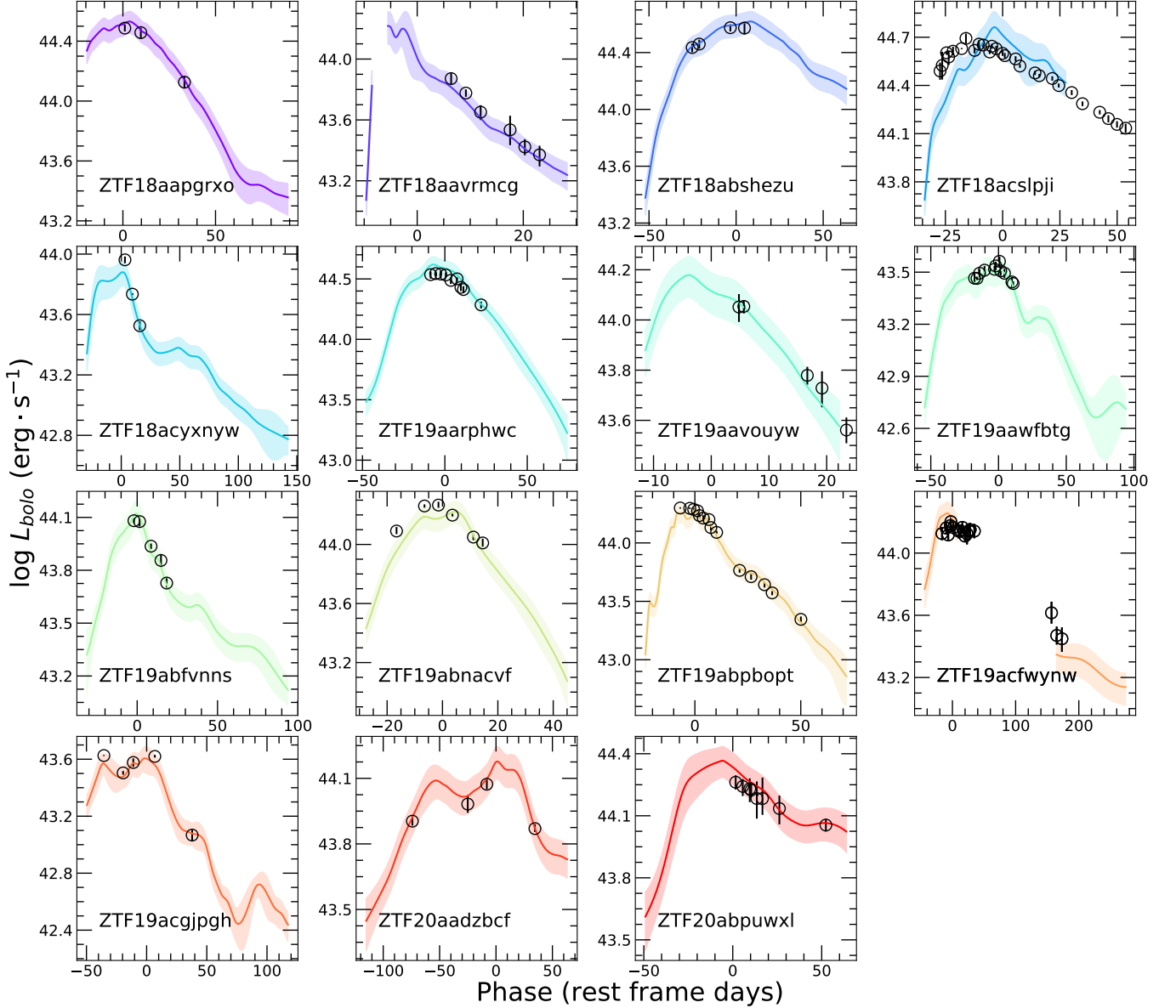


Figure 12. Bolometric LCs for the events with at least three-epoch UV photometry. The black points present the bolometric luminosities constructed with both UV and optical photometry. The bolometric LCs derived from g - and r -band photometry are shown in solid lines with 1σ error marked by the shaded area. The breaks in LCs are due to the lack of data (*e.g.* ZTF19acfwynw) or that the $(g - r)$ color is 0.1 mag beyond the range where the bolometric correction is reliable (*e.g.* ZTF18aavrmcg).

a simple conversion between the optical g and r photometry to the bolometric luminosity for low- z SLSNe-I.

ACKNOWLEDGMENTS

We acknowledge very helpful discussions about LC fitting using CSM models with Dr. Weili Lin from Tsinghua University.

Based on observations obtained with the Samuel Oschin Telescope 48-inch and the 60-inch Telescope at

the Palomar Observatory as part of the Zwicky Transient Facility project. ZTF is supported by the National Science Foundation under Grant No. AST-1440341 and a collaboration including Caltech, IPAC, the Weizmann Institute for Science, the Oskar Klein Center at Stockholm University, the University of Maryland, the University of Washington, Deutsches Elektronen-Synchrotron and Humboldt University, Los Alamos National Laboratories, the TANGO Consortium of Taiwan, the University of Wisconsin at Milwaukee, and Lawrence Berkeley National Laboratories. Operations

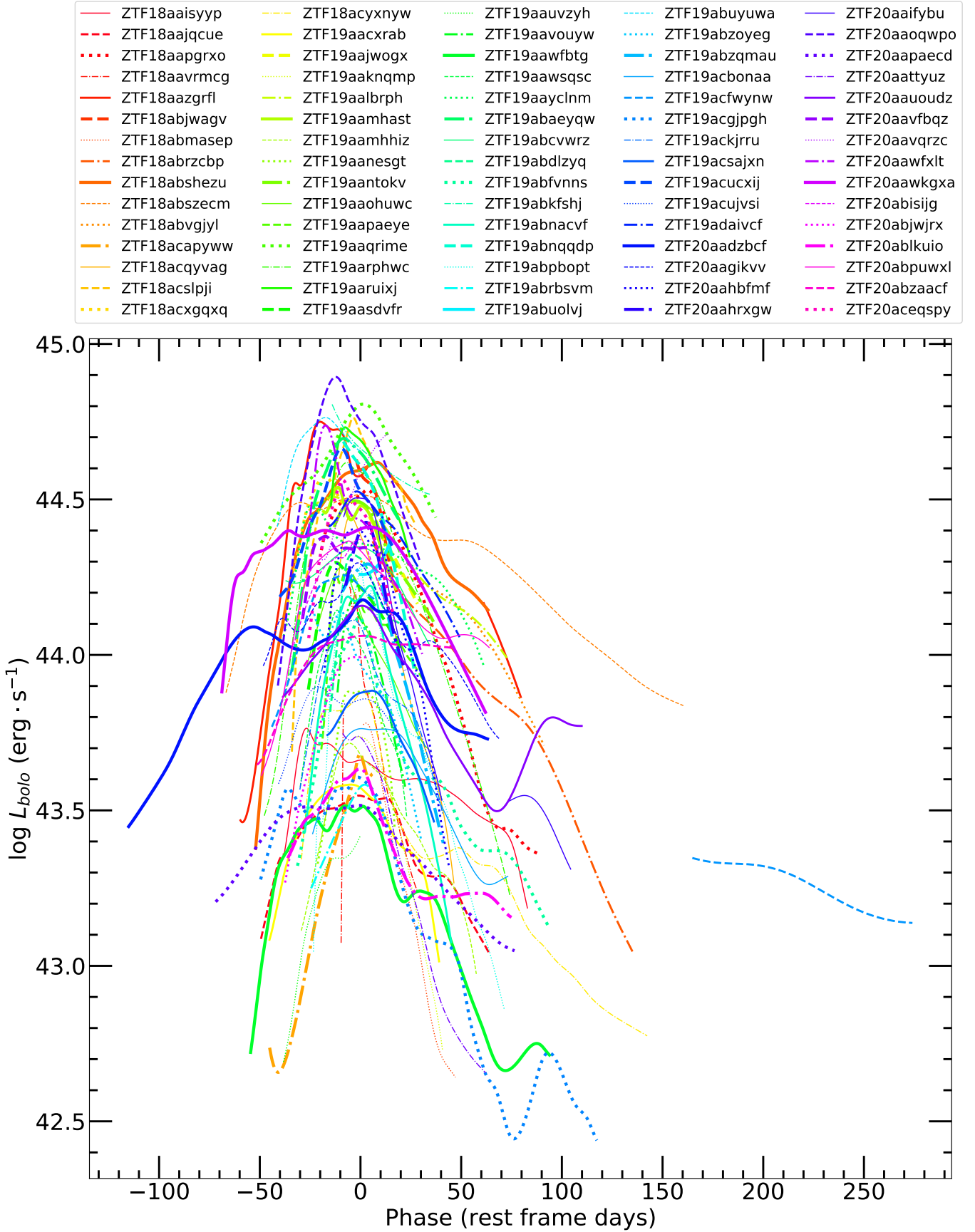


Figure 13. The derived bolometric LCs from g - and r -band photometry for our whole sample. Due to the LC quality, ZTF19aauioref and ZTF19acvxquk are excluded. The LCs are plotted in different colors, line styles and widths.

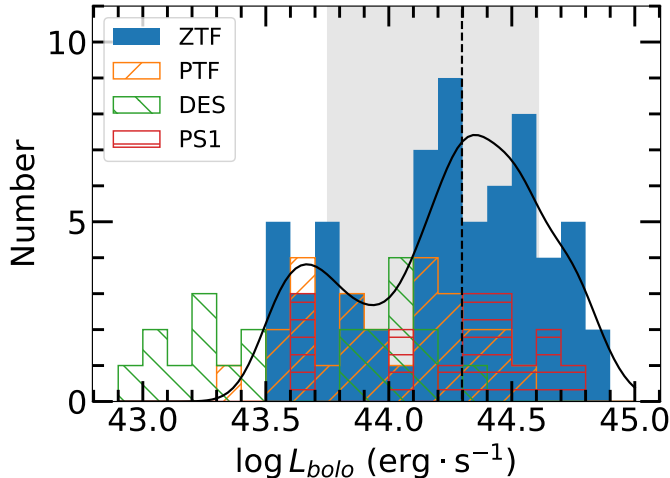


Figure 14. The distribution of the peak bolometric luminosities. The black dashed line and the gray region show the median value and the 1σ dispersion of $1.98^{+2.07}_{-1.42} \times 10^{44} \text{ erg s}^{-1}$. The black solid line shows the kernel density estimation of the distribution. The SLSN-I samples from PTF (De Cia et al. 2018), DES (Angus et al. 2019) and PS1 (Lunnan et al. 2018) are plotted in different hatching patterns for comparison.

are conducted by COO, IPAC, and UW. SED Machine is based upon work supported by the National Science Foundation under Grant No. 1106171. The ZTF forced-photometry service was funded under the Heising-Simons Foundation grant #12540303 (PI: Graham).

The Liverpool Telescope is operated on the island of La Palma by Liverpool John Moores University in the Spanish Observatorio del Roque de los Muchachos of the Instituto de Astrofísica de Canarias with financial support from the UK Science and Technology Facilities Council. The Nordic Optical Telescope is owned in collaboration by the University of Turku and Aarhus University, and operated jointly by Aarhus University, the University of Turku and the University of Oslo, representing Denmark, Finland and Norway, the University of Iceland and Stockholm University at the Observatorio del Roque de los Muchachos, La Palma, Spain, of the Instituto de Astrofísica de Canarias. This research has made use of data obtained through the High Energy Astrophysics Science Archive Research Center Online Service, provided by the NASA/Goddard Space Flight Center. This work was supported by the GROWTH project funded by the National Science Foundation under Grant No. 1545949.

S. Schulze acknowledges support from the G.R.E.A.T research environment, funded by *Vetenskapsrådet*, the Swedish Research Council, project number 2016-06012. R. L. acknowledges support from a Marie Skłodowska-

Curie Individual Fellowship within the Horizon 2020 European Union (EU) Framework Programme for Research and Innovation (H2020-MSCA-IF-2017-794467). A. Gal-Yam acknowledges support from the EU via ERC grant No. 725161, the ISF GW excellence center, an IMOS space infrastructure grant and BSF/Transformative and GIF grants, as well as the André Deloro Institute for Advanced Research in Space and Optics, the Schwartz/Reisman Collaborative Science Program and the Norman E Alexander Family M Foundation ULTRASAT Data Center Fund, Minerva and Yeda-Sela. The work of X. Wang is supported by the National Natural Science Foundation of China (NSFC grants 12033003 and 11633002), the Major State Basic Research Development Program (grant 2016YFA0400803), the Scholar Program of Beijing Academy of Science and Technology (DZ:BS202002), and the Tencent XPLOER Prize.

Facilities: PO:1.2m, PO:Hale, Liverpool:2m, NOT:2.56m, Keck:I, WHT:4.2m

Software: Scikit-learn (Pedregosa et al. 2011), *FIREFLY* (Wilkinson et al. 2017), *george* (Ambikasaran et al. 2015), *heasoft* (<https://heasarc.nasa.gov/lheasoft/>)

APPENDIX

A. INFORMATION ON THE ZTF SLSN-I SAMPLE

Table A1. The ZTF SLSN-I Sample

ZTF Name	IAU Name	RA ^a	DEC ^a	Redshift	$E(B - V)^b$ (mag)	Discovery group	Template	Spectrum Phase ^c	Template Phase ^c	Template Type
ZTF18aaisyyp	SN2018avk	13:11:27.72	+65:38:16.7	0.132	0.011	Gaia	PTF12gty	-13.37	-7.0	SLSN-I
ZTF18aajqcue	SN2018don	13:55:08.65	+58:29:42.0	0.0735	0.0089	PS1	SN2007gr	-2.18	-7.0	Ic
ZTF18aapgrxo	SN2018bym	18:43:13.42	+45:12:28.2	0.2744	0.0517	ATLAS	PTF13ajg	5.37	8.0	SLSN-I
ZTF18aavrmcg	SN2018bgv	11:02:30.29	+55:35:55.8	0.0795	0.0074	Gaia	SN2011ke	17.98	20.0	SLSN-I
ZTF18aazgrfl	SN2018lzv	12:44:02.32	+56:01:44.5	0.434	0.0081	ZTF	PTF09atu	-20.03	-20.0	SLSN-I
ZTF18abjwagv	SN2018gbw	15:55:38.02	+28:21:38.0	0.3454	0.0386	PS1	PTF13ajg	-4.44	-4.0	SLSN-I
ZTF18abmasep	SN2018fcg	21:09:36.78	+33:28:59.6	0.1011	0.1435	ZTF	PTF12dam	-4.3	-22.0	SLSN-I
ZTF18abrzcbp	SN2018lzw	07:39:32.76	+27:44:02.7	0.3198	0.0373	ZTF	PTF10uhf	27.64	15.0	SLSN-I
ZTF18abshezu	SN2018gft	23:57:17.95	-15:37:53.3	0.2320	0.0256	ZTF	PTF09cnd	-36.98	-14.0	SLSN-I
ZTF18abszecm	SN2018lzx	22:29:27.24	+13:10:39.8	0.4373	0.0529	ZTF	PTF09cnd	19.95	37.0	SLSN-I
ZTF18abvgjyl	SN2018gkz	07:58:11.54	+19:31:07.9	0.2405	0.036	ZTF	SN2007bi	19.74	50.0	SLSN-I
ZTF18acapyww	SN2018hpq	18:28:41.24	+75:48:47.3	0.124	0.0868	Gaia	PTF10nmn	25.01	0.0	SLSN-I
ZTF18acenqto	SN2018ibb	04:38:56.93	-20:39:44.2	0.166	0.0275	ATLAS				
ZTF18acqyvag	SN2018lfe	09:33:29.56	+00:03:08.4	0.3505	0.0286	PS1	SN2011ke	59.49	53.0	SLSN-I
ZTF18acslpji	SN2018hti	03:40:53.77	+11:46:37.9	0.0613	0.3983	ATLAS	PTF12dam	22.14	7.0	SLSN-I
ZTF18acxgqxq	SN2018lfd	23:14:59.32	+48:45:27.6	0.2686	0.1506	ZTF	PTF12dam	-12.72	-22.0	SLSN-I
ZTF18acyxnyw	SN2018kyt	12:27:56.23	+56:23:35.6	0.1080	0.0091	ZTF	PTF10hgi	45.14	47.0	SLSN-I
ZTF19aacxrab	SN2019J	10:03:46.78	+06:46:24.7	0.1346	0.0229	PS1	PTF10gyb	9.94	-6.0	SLSN-I
ZTF19aajwogx	SN2019cca	12:02:50.91	-16:39:53.6	0.4103	0.0462	ZTF	PTF10uhf	28.51	15.0	SLSN-I
ZTF19aaknqmp	SN2019bgu	09:57:15.34	+32:00:05.6	0.1480	0.0123	ATLAS	PTF12gty	16.59	-7.0	SLSN-I
ZTF19aalbrph	SN2019kwq	17:07:58.84	+58:42:03.9	0.49★	0.0257	ZTF	PTF09cnd	67.88	37.0	SLSN-I
ZTF19aamhast	SN2019dgr	09:45:32.68	+04:56:02.2	0.3815	0.0348	ATLAS	PTF13ajg	13.29	8.0	SLSN-I
ZTF19aamhhiz	SN2019kws	14:15:04.46	+50:39:06.8	0.1977	0.0142	ZTF	PTF12gty	21.22	-7.0	SLSN-I
ZTF19aanesgt	SN2019cdt	08:17:53.90	+65:28:46.7	0.153	0.0441	ZTF	PTF10nmn	11.46	29.0	SLSN-I
ZTF19aantokv	SN2019aamp	14:37:49.27	+20:18:16.6	0.4040	0.0237	ZTF	PTF13ajg	10.1	8.0	SLSN-I
ZTF19aaohuwc	SN2019dlr	11:17:34.18	+00:30:02.6	0.26★	0.0309	ZTF	SN2004aw	57.07	11.0	Ic
ZTF19aapaeye	SN2019cwu	14:51:37.29	+48:59:13.7	0.32★	0.0186	ZTF	SN2011ke	27.18	20.0	SLSN-I
ZTF19aaqrime	SN2019kwt	19:39:22.59	+78:45:43.8	0.3562	0.0775	ZTF	SN2007bi	12.29	50.0	SLSN-I
ZTF19aarpnwc	SN2019eot	18:00:29.95	+50:17:43.3	0.3057	0.0366	ZTF	PTF13ajg	-13.62	-4.0	SLSN-I
ZTF19aaruijx	SN2019kwu	13:57:39.77	+64:21:18.6	0.60★	0.0138	ZTF	PTF10vqv	28.18	11.0	SLSN-I
ZTF19aasdvfr	SN2019gqi	14:21:11.98	+28:54:05.9	0.3642	0.0129	ATLAS	PTF11rks	20.81	7.0	SLSN-I
ZTF19aauioref	SN2019ffy	14:05:46.73	+33:27:38.3	0.67★	0.0142	PS1	PTF09atu	16.03	28.0	SLSN-I
ZTF19aauvzyh	SN2019gam	10:19:18.32	+17:12:42.6	0.1235	0.0272	ATLAS	SN2011ke	17.65	29.0	SLSN-I
ZTF19aavouyw	SN2019gfm	15:35:46.59	+24:03:45.0	0.1816	0.0465	PS1	PTF11rks	16.23	18.0	SLSN-I
ZTF19aawfbtg	SN2019hge	22:24:21.20	+24:47:17.1	0.0866	0.058	ZTF	PTF12dam	-25.53	2.0	SLSN-I
ZTF19aawsqsc	SN2019hno	19:39:12.95	+62:43:41.0	0.26	0.0583	ATLAS	PTF09cnd	-4.09	9.0	SLSN-I
ZTF19aayclnm	SN2019aamq	20:55:36.14	-08:40:31.4	0.386	0.0636	ZTF	PTF10bjp	6.85	8.0	SLSN-I
ZTF19abaeyqw	SN2019kcy	14:08:19.78	+08:58:01.0	0.399	0.0227	ZTF	PTF13ajg	-16.44	-4.0	SLSN-I
ZTF19abcvwrz	SN2019aamx	15:57:48.27	+27:28:03.5	0.41	0.0362	ZTF	PTF09cwl	13.19	22.0	SLSN-I
ZTF19abdlzyq	SN2019aamr	15:29:23.55	+38:06:12.6	0.42	0.0118	ZTF	PTF09cwl	8.03	22.0	SLSN-I
ZTF19abfvnns	SN2019lsq	00:04:40.58	+42:52:11.3	0.1295	0.0829	ATLAS	PTF12dam	-3.33	-22.0	SLSN-I
ZTF19abkfshj	SN2019otl	02:52:21.63	-17:48:12.4	0.500	0.0241	ZTF	PTF13ajg	10.92	-4.0	SLSN-I
ZTF19abnacvf	SN2019nhs	00:52:01.44	+07:36:59.7	0.189	0.0514	PS1	PTF13ajg	-8.61	-4.0	SLSN-I
ZTF19abnqqdp	SN2019aams	23:43:36.16	+12:29:01.0	0.6360	0.0448	ZTF	PTF13ajg	0.37	-4.0	SLSN-I
ZTF19abpbopt	SN2019neq	17:54:26.76	+47:15:40.6	0.1060	0.0334	ZTF	PTF11rks	16.14	7.0	SLSN-I

Table A1 *continued*

Table A1 (*continued*)

ZTF Name	IAU Name	RA ^a	DEC ^a	Redshift	$E(B - V)^b$ (mag)	Discovery group	Template	Spectrum Phase ^c	Template Phase ^c	Template Type
ZTF19abrbsvm	SN2019obk	22:33:54.08	-02:09:42.3	0.1656	0.048	PS1	PTF12gty	13.75	-7.0	SLSN-I
ZTF19abuolvj	SN2019qgk	22:29:57.55	-04:06:02.2	0.3468	0.054	ZTF	SN2010gx	47.25	29.0	SLSN-I
ZTF19abuyuwa	SN2019sgg	01:01:11.77	+14:01:35.4	0.5726	0.0373	ZTF	PTF13ajg	-18.65	-4.0	SLSN-I
ZTF19abzoyeg	SN2019aamt	21:15:08.00	+32:43:01.3	0.2138	0.126	ZTF	PTF12dam	13.88	7.0	SLSN-I
ZTF19abzqmau	SN2019sgh	01:12:39.42	+36:28:24.8	0.3436	0.0599	ZTF	PTF10uhf	39.84	15.0	SLSN-I
ZTF19acbonaa	SN2019stc	06:54:23.10	+17:29:31.4	0.1178	0.072	ZTF	PTF10hgi	25.88	47.0	SLSN-I
ZTF19acfwynw	SN2019szu	00:10:13.14	-19:41:32.4	0.2120	0.018	ATLAS	PTF12dam	-14.43	2.0	SLSN-I
ZTF19acgjpgh	SN2019unb	09:47:57.02	+00:49:36.0	0.0635	0.1045	ZTF	PTF10hgi	-6.83	15.0	SLSN-I
ZTF19ackjrru	SN2019ujb	09:03:15.18	+40:14:32.6	0.2008	0.0165	ZTF	PTF11rks	24.45	18.0	SLSN-I
ZTF19acsajxn	SN2019xdy	08:24:51.33	+22:10:46.0	0.2206	0.0425	ZTF	PTF10vbw	32.38	22.0	SLSN-I
ZTF19acucxij	SN2019vvc	09:13:30.13	+44:46:26.2	0.3314	0.0115	ATLAS	PTF09cwl	15.82	22.0	SLSN-I
ZTF19acvxquk	SN2019aamu	02:55:08.89	+11:27:22.4	0.2590	0.1925	ZTF	PTF12gty	8.62	-7.0	SLSN-I
ZTF19adaivcf	SN2019zbv	10:15:01.10	+43:24:53.6	0.3785	0.0119	ZTF	PTF13ajg	9.25	8.0	SLSN-I
ZTF20aahbfmf	SN2020ank	08:16:14.65	+04:19:26.9	0.2485	0.0193	ZTF	PTF13ajg	-0.68	-4.0	SLSN-I
ZTF20aaifybu	SN2020auv	16:34:12.51	+13:05:51.9	0.280	0.0565	ZTF	PTF13ajg	-2.49	8.0	SLSN-I
ZTF19acujysi	SN2019aamw	23:48:54.54	+24:59:59.8	0.24	0.0526	ZTF	PTF09cnd	133.31	121.0	SLSN-I
ZTF20aadzbcf	SN2020fvm	14:12:45.93	+34:44:16.2	0.2428	0.0129	ZTF	PTF10uhf	-1.32	15.0	SLSN-I
ZTF20aagikvv	SN2019aamv	12:45:01.65	+33:33:14.1	0.3996	0.0127	ZTF	PTF13ajg	-11.52	8.0	SLSN-I
ZTF20aahrxgw	SN2020aup	13:09:44.44	+12:29:13.4	0.31*	0.0208	ZTF	PTF09cwl	16.63	22.0	SLSN-I
ZTF20aaqwpo	SN2020dlb	08:08:34.14	+34:44:12.9	0.398	0.0327	ZTF	SN2005ap	-1.1	4.0	SLSN-I
ZTF20aapaecd	SN2020fyq	14:46:10.44	+23:48:02.0	0.1765	0.0325	PS1	SN2011ke	27.08	53.0	SLSN-I
ZTF20aattyuz	SN2020exj	14:42:40.01	+30:14:39.1	0.1216	0.0096	ATLAS	PTF10hgi	44.31	47.0	SLSN-I
ZTF20aaouodz	SN2020htd	17:44:17.28	+38:55:30.4	0.3515	0.026	PS1	PTF09cnd	7.04	13.0	SLSN-I
ZTF20aavfbqz	SN2020iyj	09:15:36.64	+53:27:32.0	0.3690	0.0155	ZTF	PTF09cwl	1.72	1.0	SLSN-I
ZTF20aavqrzc	SN2020kox	11:06:04.97	+26:17:28.7	0.456	0.0166	ATLAS	PTF13ajg	3.18	-4.0	SLSN-I
ZTF20aawfxlt	SN2020jii	15:34:55.31	+02:51:11.5	0.396	0.0427	PS1	PTF13ajg	-2.03	-4.0	SLSN-I
ZTF20aawkgxa	SN2020afah	10:20:18.32	+53:19:21.4	0.3754	0.0086	ZTF	PTF09cnd	-44.28	-16.0	SLSN-I
ZTF20abisijg	SN2020afag	00:15:46.25	+47:00:08.5	0.3815	0.0898	ZTF	PTF09cwl	6.84	22.0	SLSN-I
ZTF20abjwrx	SN2020onb	14:23:00.61	+49:10:40.7	0.16*	0.0208	ZTF	SN2004aw	25.25	4.0	Ic
ZTF20ablkuio	SN2020qef	22:56:10.53	+28:45:53.3	0.1831	0.0459	ATLAS	PTF12gty	24.32	-7.0	SLSN-I
ZTF20abpuwxi	SN2020rmv	00:40:00.19	-14:35:25.1	0.2621	0.0185	ATLAS	PTF10uhf	11.54	15.0	SLSN-I
ZTF20abzaacf	SN2020xkv	22:37:46.00	+23:31:37.4	0.2410	0.0303	ATLAS	SN2011ke	-11.35	20.0	SLSN-I
ZTF20aceqspy	SN2020xgd	00:19:45.83	+05:08:18.7	0.455	0.0145	PS1	PTF13ajg	-4.68	-4.0	SLSN-I

^aIn J2000.^bFrom Schlafly & Finkbeiner (2011).^cIn rest-frame days.* means the redshift is fit by *superfit*.**Table A2.** Photometry data

Name	MJD (days)	Filter	Mag(AB) (mag)	Error _{mag} (mag)	Label ^a	Flux _{ratio} ^b (10 ⁻⁹)	Tel.+Ins. ^c
ZTF18aaisyyp	58202.30	g	20.48	0.21	F	6.44	P48+ZTF
ZTF18aaisyyp	58202.32	g	20.64	0.18	F	5.55	P48+ZTF
ZTF18aaisyyp	58202.32	g	20.74	0.16	F	5.07	P48+ZTF
ZTF18aaisyyp	58202.34	g	20.78	0.19	F	4.88	P48+ZTF
ZTF18aaisyyp	58202.36	g	20.92	0.14	F	4.29	P48+ZTF
ZTF18aaisyyp	58202.36	g	20.80	0.21	F	4.79	P48+ZTF
ZTF18aaisyyp	58203.35	g	20.54	0.15	F	6.09	P48+ZTF
ZTF18aaisyyp	58204.39	g	20.10	0.19	F	9.13	P48+ZTF

^aF means real detection and T means upper limit.^bThe ratio of observed flux and flux zero point.^cTelescope+Instrument.

(This table is available in its entirety in machine-readable form.)

Table A3. LC properties

Name	K-correction ^a (mag)	M_{peak} (mag)	L_{peak} ($10^{43} \text{ erg s}^{-1}$)	t_{peak} (MJD)	$t_{rise,1/2}$ (days)	$t_{decay,1/2}$ (days)	$t_{rise,10\%}$ (days)
ZTF18aaisyyp	-0.00	-20.38 ± 0.02	5.8 ± 1.1	$58257.13^{+5.42}_{-4.50}$	$38.09^{+4.82}_{-4.02}$	$65.07^{+4.90}_{-6.40}$	$50.29^{+5.03}_{-4.05}$
ZTF18aajqcue	0.09	-20.10 ± 0.01	3.5 ± 0.6	$58280.34^{+3.57}_{-3.55}$	$44.29^{+3.35}_{-3.33}$	$24.42^{+3.36}_{-3.36}$	-
ZTF18aapgrxo	-0.22	-22.10 ± 0.01	34.0 ± 5.7	$58274.15^{+1.80}_{-1.80}$	$20.20^{+1.51}_{-1.46}$	$36.45^{+1.43}_{-1.44}$	-
ZTF18aavrmcg	-0.09	-20.72 ± 0.02	$(16.5 \pm 4.0)^b$	$58253.59^{+1.32}_{-1.71}$	$7.46^{+1.23}_{-1.59}$	$15.21^{+1.62}_{-1.33}$	$9.84^{+1.23}_{-1.59}$
ZTF18aazgrfl	-0.39	-22.32 ± 0.05	56.2 ± 18.6	$58341.73^{+14.06}_{-9.90}$	$37.33^{+9.85}_{-6.98}$	$55.25^{+8.45}_{-19.24}$	$48.76^{+9.87}_{-6.96}$
ZTF18abjwagv	-0.33	-22.17 ± 0.03	(42.5 ± 7.6)	$58348.97^{+4.52}_{-3.18}$	$19.72^{+3.47}_{-2.50}$	$20.37^{+3.41}_{-3.65}$	$33.02^{+3.59}_{-2.74}$
ZTF18abmasep	-0.13	-20.43 ± 0.02	(6.0 ± 1.0)	$58355.73^{+2.78}_{-2.44}$	$11.54^{+2.53}_{-2.22}$	$14.79^{+2.23}_{-2.53}$	$17.71^{+2.64}_{-2.26}$
ZTF18abrzcbb	-0.30*	(-21.82 ± 0.04)	(23.2 ± 4.9)	$(58360.51^{+3.40}_{-0})$	-	$(48.46^{+1.26}_{-2.92})$	-
ZTF18abshezu	-0.18	-22.29 ± 0.02	41.6 ± 7.3	$58418.56^{+5.88}_{-5.01}$	$31.13^{+4.78}_{-4.08}$	-	$48.59^{+4.89}_{-4.14}$
ZTF18abszecm	-0.44	-22.10 ± 0.02	32.8 ± 5.7	$58436.32^{+8.34}_{-7.49}$	$54.52^{+5.86}_{-5.28}$	$94.51^{+8.67}_{-12.83}$	$75.92^{+6.31}_{-5.66}$
ZTF18abvgjyl	-0.24	(-21.87 ± 0.02)	(20.0 ± 3.9)	$(58372.52^{+5.45}_{-0})$	-	$(78.61^{+1.49}_{-4.62})$	-
ZTF18acapyyw	-0.13*	-20.24 ± 0.02	4.8 ± 0.8	$58427.88^{+0.86}_{-1.13}$	$14.02^{+4.28}_{-4.06}$	-	$32.07^{+1.35}_{-2.04}$
ZTF18acqvvag	-0.33*	-21.58 ± 0.04	28.0 ± 9.1	$58465.66^{+3.75}_{-6.58}$	$15.17^{+3.08}_{-5.07}$	$20.89^{+6.36}_{-4.61}$	-
ZTF18acslpji	-0.09	-22.20 ± 0.02	57.8 ± 14.6	$58459.50^{+4.70}_{-4.11}$	$23.23^{+4.45}_{-3.89}$	-	$34.76^{+4.46}_{-3.89}$
ZTF18acxgqxq	-0.19	-22.14 ± 0.09	37.5 ± 8.1	$58503.13^{+21.34}_{-6.53}$	$33.80^{+16.86}_{-5.28}$	-	-
ZTF18acyxnyw	-0.13	-20.61 ± 0.04	$9.2 \pm 0.5 \star \star$	$58506.99^{+3.40}_{-5.48}$	$25.18^{+3.34}_{-5.03}$	$16.91^{+5.10}_{-3.12}$	$33.70^{+3.08}_{-4.95}$
ZTF19aacxrab	-0.05	-19.97 ± 0.11	3.8 ± 1.0	$58545.72^{+10.13}_{-18.66}$	$39.78^{+9.23}_{-16.75}$	$26.47^{+16.63}_{-9.23}$	$53.70^{+9.06}_{-16.53}$
ZTF19aajwogx	-0.37*	-22.06 ± 0.07	(27.9 ± 5.3)	$58559.79^{+6.68}_{-10.02}$	$28.04^{+7.95}_{-8.03}$	$31.42^{+7.36}_{-4.90}$	-
ZTF19aaknqmp	-0.14	-20.41 ± 0.10	5.5 ± 1.3	$58559.95^{+4.26}_{-10.71}$	-	$18.41^{+9.42}_{-3.91}$	-
ZTF19aalbrph	-0.43*	-22.08 ± 0.03	32.2 ± 5.5	$58564.85^{+5.61}_{-7.87}$	$39.57^{+6.31}_{-6.87}$	$47.73^{+6.89}_{-6.85}$	$62.13^{+11.13}_{-9.01}$
ZTF19aamhast	-0.37	-21.96 ± 0.07	34.6 ± 10.5	$58581.64^{+5.08}_{-7.58}$	$20.84^{+3.87}_{-5.63}$	-	$36.33^{+3.86}_{-5.89}$
ZTF19aamhhiz	-0.31	-20.13 ± 0.02	5.2 ± 0.9	$58574.58^{+4.94}_{-3.96}$	$19.38^{+4.25}_{-3.44}$	$45.77^{+3.63}_{-4.40}$	-
ZTF19aanesgt	-0.04	-20.90 ± 0.02	7.7 ± 1.3	$58583.79^{+1.73}_{-6.57}$	$14.95^{+1.59}_{-5.71}$	$11.09^{+5.70}_{-1.53}$	$27.07^{+5.66}_{-6.29}$
ZTF19aantokv	-0.40	-21.94 ± 0.02	31.3 ± 5.5	$58585.82^{+4.57}_{-7.36}$	-	$39.05^{+5.95}_{-3.69}$	-
ZTF19aaohuwc	-0.24	-21.20 ± 0.05	19.1 ± 4.2	$58594.10^{+6.05}_{-7.21}$	$24.98^{+5.18}_{-5.97}$	$30.53^{+6.40}_{-5.52}$	$39.36^{+9.14}_{-6.69}$
ZTF19aapaeye	-0.30	-21.34 ± 0.02	18.9 ± 3.5	$58600.12^{+4.48}_{-3.83}$	$16.46^{+3.40}_{-2.91}$	$41.93^{+3.91}_{-4.56}$	$21.42^{+3.45}_{-2.93}$
ZTF19aaqrime	-0.34	-22.86 ± 0.02	64.1 ± 11.1	$58649.33^{+4.22}_{-4.03}$	$41.53^{+3.58}_{-3.38}$	$38.59^{+3.13}_{-3.24}$	$69.16^{+7.69}_{-4.16}$
ZTF19aarphwc	-0.28	-22.20 ± 0.01	41.5 ± 7.0	$58644.78^{+2.40}_{-2.39}$	$27.12^{+1.85}_{-1.85}$	$32.16^{+2.03}_{-2.01}$	$41.05^{+2.07}_{-1.98}$
ZTF19aaruijx	-0.51*	-22.41 ± 0.07	53.9 ± 9.8	$58620.92^{+5.10}_{-3.18}$	$12.54^{+3.21}_{-2.02}$	$23.73^{+2.44}_{-3.47}$	$20.41^{+3.29}_{-2.18}$
ZTF19aasdvfr	-0.34*	-21.54 ± 0.03	19.8 ± 4.9	$58637.61^{+4.58}_{-4.50}$	$23.68^{+3.46}_{-3.40}$	-	$35.34^{+3.82}_{-3.73}$
ZTF19aauioref	-0.69	-22.88 ± 0.03	-	$58640.23^{+5.13}_{-5.65}$	$20.50^{+3.11}_{-3.42}$	-	$30.42^{+4.66}_{-3.93}$
ZTF19aauvzyh	0.32	(-19.98 ± 0.11)	(2.6 ± 0.7)	$(58648.17^{+0}_{-4.09})$	$(21.84^{+2.43}_{-4.37})$	-	$(38.93^{+1.21}_{-3.81})$
ZTF19aavouyw	-0.02	-21.07 ± 0.03	15.1 ± 2.8	$58645.82^{+3.49}_{-2.17}$	$12.14^{+3.01}_{-1.90}$	$22.37^{+2.09}_{-3.09}$	$21.54^{+3.44}_{-2.66}$
ZTF19aawfbtg	-0.11	-19.90 ± 0.02	$3.7 \pm 0.2 \star \star$	$58693.74^{+3.46}_{-8.54}$	$42.69^{+3.23}_{-7.88}$	$17.35^{+7.89}_{-3.26}$	$57.16^{+15.62}_{-7.99}$
ZTF19aawsqsc	-0.21	-21.14 ± 0.03	13.9 ± 2.6	$58671.15^{+2.69}_{-8.17}$	$26.13^{+2.23}_{-6.52}$	$18.06^{+6.62}_{-2.59}$	$35.18^{+2.65}_{-6.56}$
ZTF19aayclnm	-0.36	-21.88 ± 0.03	30.8 ± 10.4	$58686.50^{+5.40}_{-7.21}$	$38.28^{+4.51}_{-5.61}$	$57.35^{+5.43}_{-4.32}$	-
ZTF19abaeyqw	-0.41	-22.13 ± 0.10	49.7 ± 13.0	$58689.99^{+13.57}_{-10.18}$	$26.92^{+9.74}_{-7.32}$	-	$40.00^{+9.94}_{-7.39}$
ZTF19abcvwrz	-0.33	-21.90 ± 0.07	22.3 ± 4.7	$58709.40^{+8.66}_{-11.74}$	$37.81^{+6.29}_{-8.42}$	$33.95^{+8.60}_{-6.37}$	$50.66^{+6.20}_{-8.38}$
ZTF19abdlyzq	-0.41	-21.46 ± 0.08	21.1 ± 4.5	$58684.60^{+6.25}_{-3.60}$	$12.06^{+4.43}_{-2.59}$	$23.96^{+3.58}_{-5.03}$	$17.71^{+4.42}_{-2.56}$
ZTF19abfvnns	-0.22	-21.00 ± 0.01	13.2 ± 2.3	$58707.76^{+1.39}_{-1.43}$	$17.64^{+1.26}_{-1.29}$	$19.94^{+1.52}_{-1.41}$	$31.34^{+1.60}_{-1.44}$
ZTF19abkfshj	-0.46	-22.45 ± 0.04	(63.9 ± 14.6)	$58715.61^{+11.71}_{-14.09}$	-	-	-
ZTF19abnacvf	-0.05	-21.49 ± 0.03	$18.5 \pm 0.9 \star \star$	$58732.23^{+3.73}_{-5.21}$	$19.94^{+3.18}_{-4.42}$	$22.60^{+4.40}_{-3.16}$	$30.63^{+3.51}_{-4.51}$
ZTF19abnqqdp	-0.60	-22.23 ± 0.04	(48.5 ± 14.0)	$58731.39^{+8.12}_{-4.13}$	$21.15^{+5.35}_{-3.00}$	$20.04^{+3.31}_{-5.96}$	$33.89^{+7.89}_{-4.94}$
ZTF19abpbopt	-0.24	-21.40 ± 0.01	$19.9 \pm 0.2 \star \star$	$58730.14^{+0.88}_{-0.91}$	$12.85^{+0.80}_{-0.83}$	$16.16^{+0.84}_{-0.80}$	$21.91^{+0.81}_{-0.84}$
ZTF19abrbsvm	-0.10	-19.87 ± 0.07	3.8 ± 1.2	$58733.97^{+11.43}_{-9.37}$	$28.89^{+10.44}_{-8.58}$	-	$54.47^{+11.46}_{-11.92}$
ZTF19abuolvj	-0.32*	(-21.66 ± 0.07)	(23.1 ± 6.6)	$(58744.36^{+9.28}_{-0})$	-	$(38.29^{+4.67}_{-8.42})$	-
ZTF19abuyuwa	-0.42	(-22.42 ± 0.05)	58.0 ± 11.1	$(58791.33^{+0}_{-5.81})$	$(38.31^{+1.10}_{-3.91})$	-	$(51.67^{+1.60}_{-3.97})$
ZTF19abzoyeg	-0.24	-20.84 ± 0.03	13.9 ± 3.1	$58775.15^{+5.64}_{-7.57}$	$23.35^{+4.66}_{-6.25}$	$24.76^{+6.39}_{-4.90}$	$34.63^{+4.72}_{-6.27}$
ZTF19abzqmau	-0.34	-21.40 ± 0.02	19.6 ± 3.5	$58758.47^{+7.14}_{-3.73}$	$12.77^{+5.33}_{-2.80}$	$27.45^{+7.96}_{-8.62}$	$18.56^{+5.87}_{-3.12}$
ZTF19acbonaa	-0.02	-20.62 ± 0.02	5.8 ± 1.0	$58783.07^{+10.81}_{-4.97}$	$21.32^{+9.71}_{-4.52}$	$32.99^{+5.15}_{-9.89}$	-

Table A3 continued

Table A3 (*continued*)

Name	K-correction ^a (mag)	M_{peak} (mag)	L_{peak} (10^{43} erg s ⁻¹)	t_{peak} (MJD)	$t_{rise,1/2}$ (days)	$t_{decay,1/2}$ (days)	$t_{rise,10\%}$ (days)
ZTF19acfwynw	-0.06	-21.33 ± 0.04	18.0 ± 3.4	$58828.49^{+7.09}_{-9.86}$	$43.67^{+7.54}_{-8.77}$	-	-
ZTF19acgjpgh	-0.03	-20.19 ± 0.04	$4.2 \pm 0.0 \star \star$	$58842.27^{+3.96}_{-4.06}$	$48.83^{+3.74}_{-3.83}$	$17.62^{+3.86}_{-3.77}$	-
ZTF19ackjrru	-0.05	-21.19 ± 0.07	12.9 ± 2.9	$58819.64^{+6.03}_{-9.07}$	$23.87^{+5.04}_{-7.56}$	$44.91^{+7.57}_{-5.06}$	$36.23^{+7.62}_{-7.84}$
ZTF19acsajxn	-0.22 \star	-20.80 ± 0.03	7.7 ± 3.4	$58832.48^{+3.13}_{-5.25}$	$21.48^{+3.16}_{-4.79}$	$32.59^{+4.31}_{-2.58}$	$38.08^{+5.93}_{-5.08}$
ZTF19acucxij	-0.31 \star	-22.16 ± 0.03	46.1 ± 19.0	$58859.94^{+3.33}_{-3.43}$	$36.21^{+2.72}_{-2.92}$	-	$53.31^{+5.11}_{-4.76}$
ZTF19acvxquk	-0.25 \star	(-21.78 ± 0.08)	-	$(58861.15^{+0}_{-6.10})$	$(38.66^{+1.90}_{-5.26})$	-	$(65.58^{+1.06}_{-4.92})$
ZTF19adaivcf	-0.39	-22.07 ± 0.02	33.6 ± 5.7	$58868.25^{+3.33}_{-3.45}$	$23.17^{+2.49}_{-2.57}$	$43.75^{+3.54}_{-3.69}$	-
ZTF20aahbfmf	-0.22	-21.83 ± 0.01	25.3 ± 4.6	$58893.85^{+3.63}_{-2.07}$	$13.47^{+2.92}_{-1.68}$	$27.25^{+2.60}_{-3.38}$	$23.17^{+3.83}_{-2.39}$
ZTF20aaifybu	-0.21	-21.94 ± 0.05	32.0 ± 6.8	$58884.18^{+5.01}_{-5.62}$	-	$21.29^{+4.43}_{-3.94}$	-
ZTF19acujvsi	-0.23 \star	-20.78 ± 0.04	7.9 ± 1.5	$58856.70^{+7.32}_{-8.76}$	$39.05^{+6.00}_{-7.15}$	$40.42^{+12.09}_{-6.90}$	$64.51^{+6.07}_{-7.38}$
ZTF20aadzbef	-0.19	-21.50 ± 0.02	15.0 ± 2.6	$58999.65^{+4.38}_{-2.74}$	$83.37^{+3.57}_{-2.27}$	$38.67^{+2.38}_{-3.61}$	-
ZTF20aagkvv	-0.38	-21.57 ± 0.05	19.8 ± 3.7	$58920.12^{+6.07}_{-3.76}$	$45.10^{+4.81}_{-3.45}$	$50.97^{+3.29}_{-4.68}$	$66.25^{+20.62}_{-6.75}$
ZTF20aahrxgw	-0.28	-21.54 ± 0.03	26.7 ± 5.2	$58882.22^{+5.44}_{-4.60}$	$12.81^{+4.25}_{-3.61}$	$24.70^{+4.00}_{-4.27}$	$20.63^{+4.75}_{-4.05}$
ZTF20aaoqwp	-0.36 \star	-22.67 ± 0.02	78.3 ± 22.2	$58950.53^{+4.09}_{-3.12}$	$27.92^{+2.97}_{-3.12}$	$26.50^{+3.20}_{-3.06}$	$42.89^{+3.36}_{-3.20}$
ZTF20aapaecd	-0.18 \star	-20.01 ± 0.02	3.3 ± 0.6	$58966.14^{+4.09}_{-6.88}$	$63.23^{+3.83}_{-6.06}$	$48.00^{+7.37}_{-4.97}$	$86.67^{+4.59}_{-6.62}$
ZTF20aatyuz	-0.22	-20.20 ± 0.03	5.6 ± 1.1	$58946.30^{+3.63}_{-2.41}$	$16.94^{+3.48}_{-2.43}$	$18.24^{+2.15}_{-3.24}$	$26.58^{+3.43}_{-2.58}$
ZTF20aaoudz	-0.33 \star	-21.32 ± 0.02	14.4 ± 2.5	$58988.48^{+4.99}_{-4.80}$	$40.71^{+5.37}_{-4.80}$	$36.85^{+3.71}_{-3.93}$	$66.00^{+4.76}_{-4.19}$
ZTF20aavfbqz	-0.35	-21.80 ± 0.03	24.0 ± 4.3	$58995.65^{+6.61}_{-7.12}$	$26.65^{+4.86}_{-5.23}$	$45.99^{+29.10}_{-13.82}$	$39.35^{+4.98}_{-5.32}$
ZTF20aavqrzc	-0.36	-21.92 ± 0.06	(51.6 ± 15.5)	$58993.37^{+8.02}_{-9.59}$	$23.02^{+5.62}_{-6.70}$	$65.86^{+18.17}_{-16.26}$	$34.12^{+5.80}_{-6.79}$
ZTF20aawfxlt	-0.40	-21.98 ± 0.03	54.7 ± 19.8	$59000.84^{+3.99}_{-3.77}$	$25.49^{+3.07}_{-2.88}$	$25.82^{+2.97}_{-3.17}$	$39.73^{+3.33}_{-3.28}$
ZTF20aawkgxa	-0.35 \star	-21.99 ± 0.06	25.8 ± 11.6	$59058.90^{+19.97}_{-7.13}$	$58.87^{+14.53}_{-5.22}$	$43.07^{+7.46}_{-17.65}$	$72.29^{+14.54}_{-5.21}$
ZTF20abisijg	-0.37	-21.76 ± 0.03	23.5 ± 4.1	$59065.55^{+3.62}_{-2.88}$	$31.42^{+2.98}_{-2.46}$	$27.94^{+3.15}_{-3.46}$	$49.59^{+6.26}_{-4.72}$
ZTF20abjwjrjx	-0.11	-21.12 ± 0.02	9.8 ± 1.7	$59077.71^{+3.04}_{-5.24}$	$23.03^{+2.69}_{-4.58}$	-	$39.57^{+2.73}_{-4.57}$
ZTF20ablkuio	-0.26	-20.18 ± 0.02	4.3 ± 0.7	$59083.23^{+2.09}_{-2.17}$	$30.99^{+1.86}_{-1.97}$	$19.44^{+2.11}_{-2.03}$	$47.81^{+2.41}_{-2.47}$
ZTF20abpuwxi	-0.18	-21.66 ± 0.02	23.2 ± 4.0	$59119.43^{+7.95}_{-6.82}$	$36.04^{+6.74}_{-6.14}$	-	$55.80^{+7.20}_{-5.64}$
ZTF20abzaacf	-0.36	-21.18 ± 0.02	11.5 ± 2.2	$59148.09^{+9.03}_{-8.06}$	$42.45^{+7.32}_{-6.54}$	-	$73.34^{+7.49}_{-6.77}$
ZTF20aceqspy	-0.45	-22.01 ± 0.06	36.5 ± 7.2	$59149.80^{+4.62}_{-3.75}$	$20.97^{+3.23}_{-2.69}$	$16.33^{+2.75}_{-3.27}$	$29.73^{+3.72}_{-2.80}$

M_{peak} , t_{peak} , $t_{rise,1/2}$, $t_{decay,1/2}$ and $t_{rise,10\%}$ are measured in the rest-frame g -band LCs.

^aK-correction to rest-frame g -band at the peak. It equals $K_{g \rightarrow g}$ for $z \leq 0.17$ and $K_{r \rightarrow g}$ for $z > 0.17$.

^bThe value in parentheses means they are not well-constrained due to the lack of data.

\star means the K-correction is calculated by $-2.5 \times \log(1+z)$.

$\star\star$ means the L_{peak} is calculated from multi-band data instead of corrected from g - and r -band flux.

Table A4. ($g-r$) colors at peak.

Name	Observed (mag)	Rest frame (mag)
ZTF18aaisyyp	-0.02 ± 0.03	-0.20 ± 0.03
ZTF18aajqcue	0.25 ± 0.02	0.09 ± 0.02
ZTF18aapgrxo	-0.12 ± 0.01	-0.31 ± 0.03
ZTF18aavrmcg	-0.27 ± 0.03	-0.29 ± 0.03
ZTF18aazgrfl	-0.03 ± 0.08	-
ZTF18abjwagv	-0.13 ± 0.04	-
ZTF18abmasep	-0.16 ± 0.02	-0.18 ± 0.02
ZTF18abshezu	-0.14 ± 0.03	-0.23 ± 0.04
ZTF18abszecm	0.02 ± 0.04	-
ZTF18acapyww	-0.11 ± 0.02	-

(This table is available in its entirety in machine-readable form.)

Table A5. Temperatures and bolometric luminosities.

Name	Phase (days)	Temperature (10^4 K)	L_{bol} (10^{43} erg s $^{-1}$)
ZTF18aaisyyp	-4.09	$5.14^{+0.57}_{-0.55}$	$1.05^{+0.15}_{-0.10}$
ZTF18aaisyyp	17.11	$4.26^{+0.42}_{-0.41}$	$0.74^{+0.05}_{-0.04}$
ZTF18aapgrxo	1.05	$30.69^{+1.66}_{-1.51}$	$1.16^{+0.07}_{-0.07}$
ZTF18aapgrxo	9.68	$28.64^{+2.26}_{-2.50}$	$1.05^{+0.09}_{-0.09}$
ZTF18aapgrxo	33.22	$13.37^{+1.21}_{-1.19}$	$0.81^{+0.06}_{-0.05}$
ZTF18aavrmcg	6.40	$7.44^{+0.68}_{-0.65}$	$1.40^{+0.34}_{-0.19}$
ZTF18aavrmcg	9.18	$5.98^{+0.34}_{-0.33}$	$1.17^{+0.10}_{-0.09}$
ZTF18aavrmcg	11.96	$4.48^{+0.50}_{-0.51}$	$0.94^{+0.12}_{-0.09}$
ZTF18aavrmcg	17.52	$3.43^{+0.82}_{-0.71}$	$0.73^{+0.49}_{-0.09}$
ZTF18aavrmcg	20.30	$2.64^{+0.33}_{-0.31}$	$0.64^{+0.05}_{-0.04}$
ZTF18aavrmcg	23.08	$2.35^{+0.35}_{-0.38}$	$0.60^{+0.09}_{-0.04}$

(This table is available in its entirety in machine-readable form.)

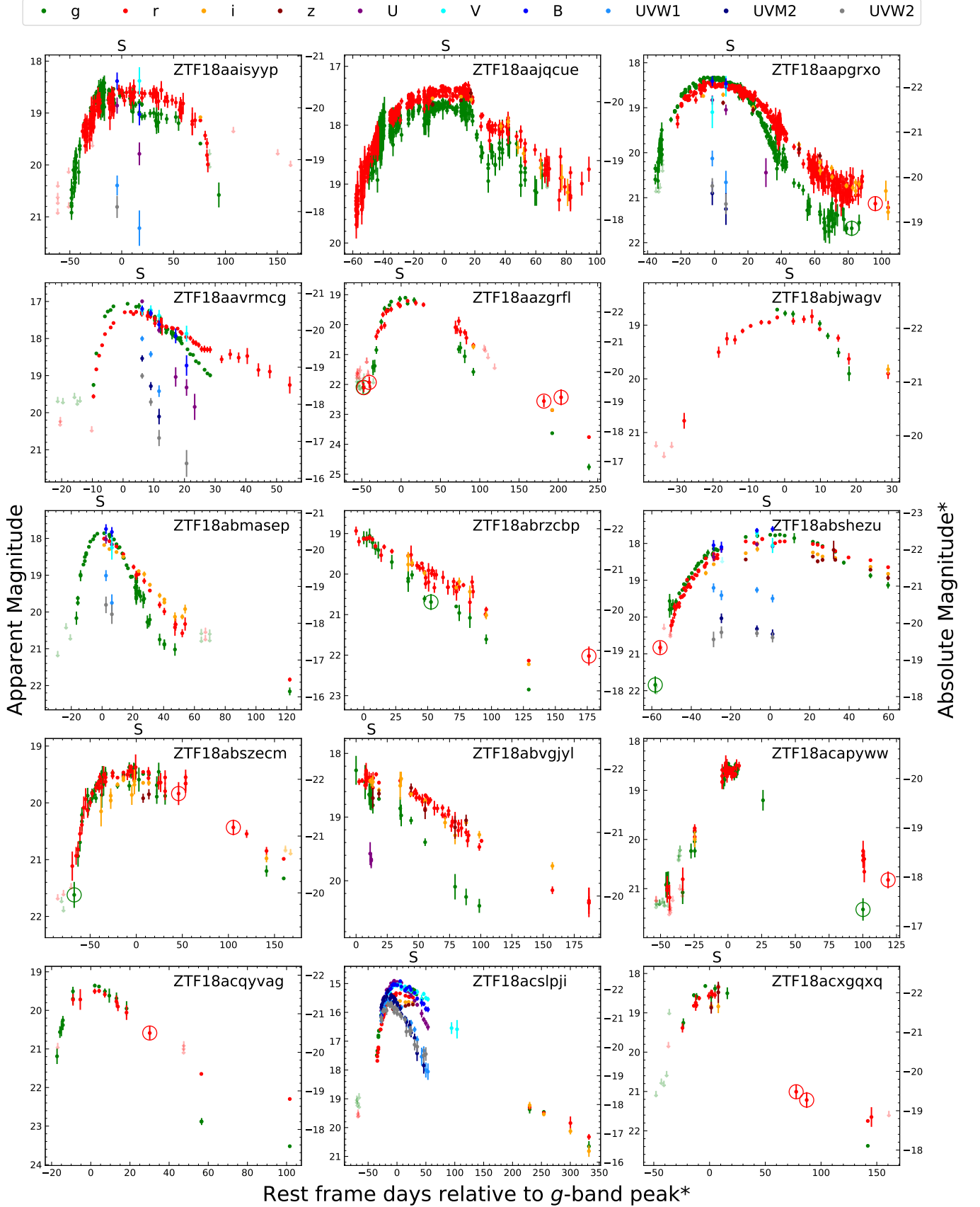


Figure A1. The LCs of our sample. All magnitudes are in the AB system and have been corrected for Milky Way extinction. The absolute magnitude y-axis on the right side is calculated by assuming a constant K-correction of $-2.5 \times \log(1+z)$. The rings mark the data measured from the combined image of multiple nearby images. The symbol 'S' at the top of each panel shows the epoch of the closest spectrum to the peak, which is used to calculate accurate K-corrections and color corrections. X-axis shows the rest-frame days relative to the observed g -band peak. ZTF18abjwagv, ZTF19aajwogx, ZTF19aauiresf, ZTF19acsajxn, ZTF19acucxij, ZTF19acvxqk and ZTF20aahbfmf are relative to r -band peak.

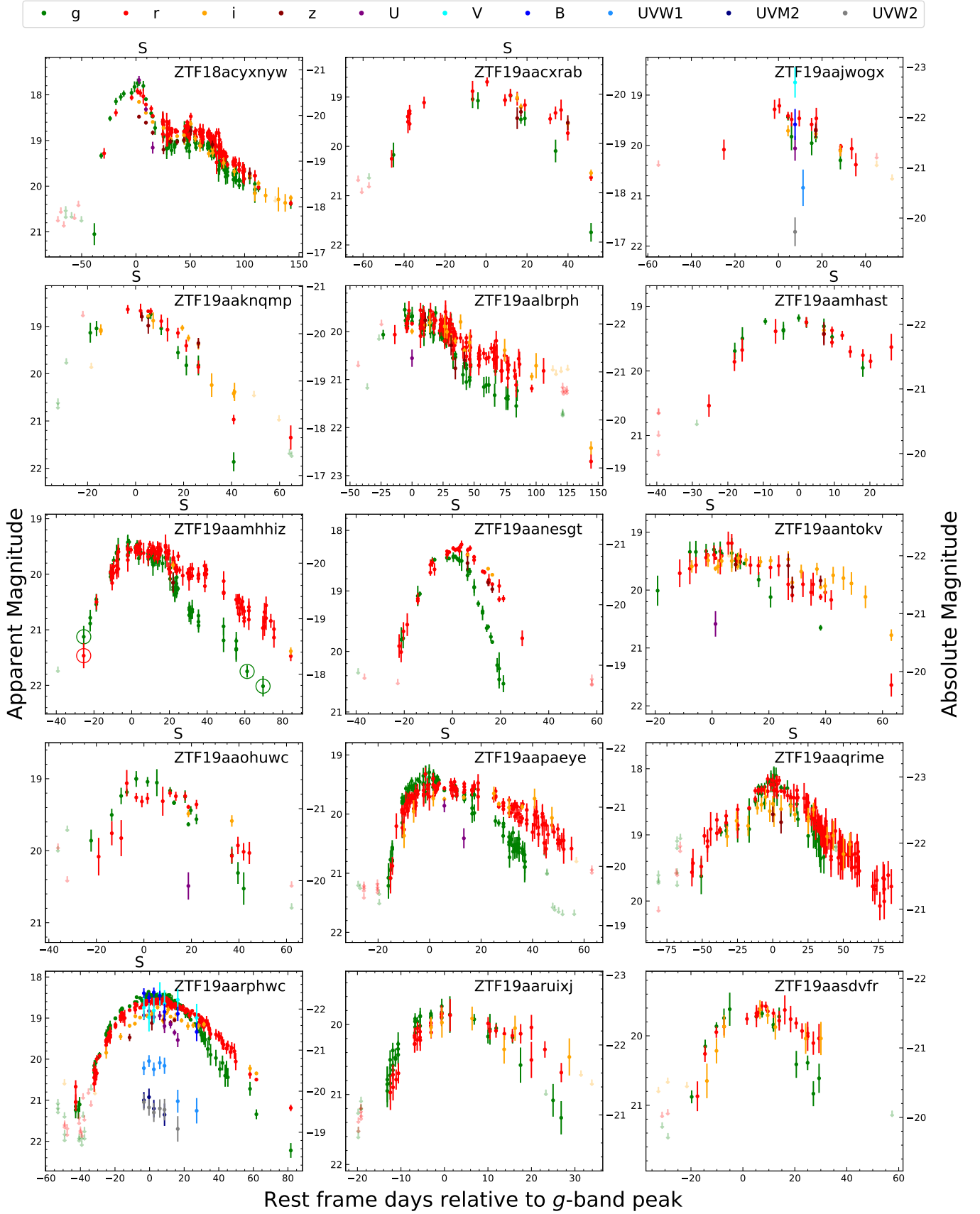


Figure A2. Similar to Figure A1.

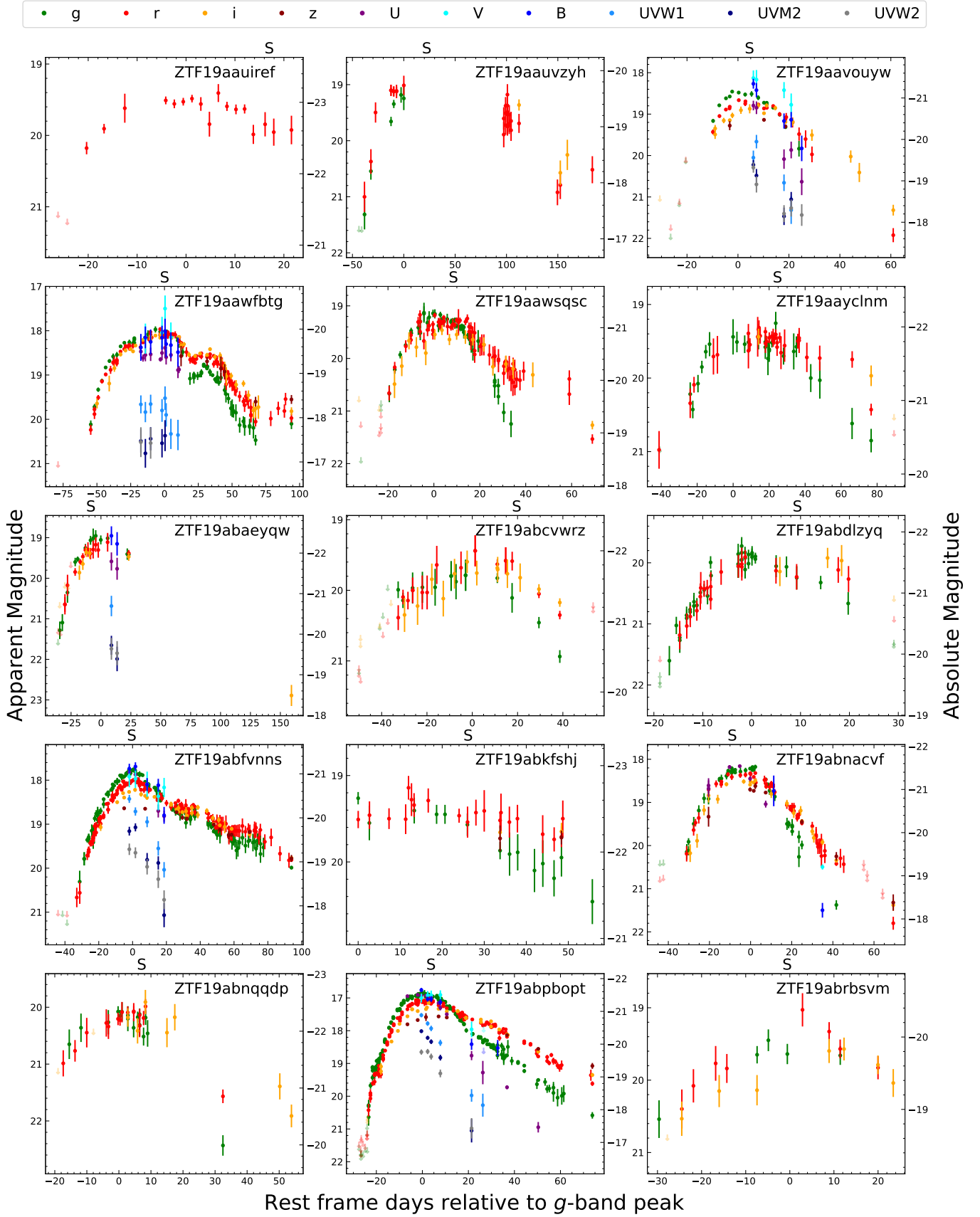


Figure A3. Similar to Figure A1.

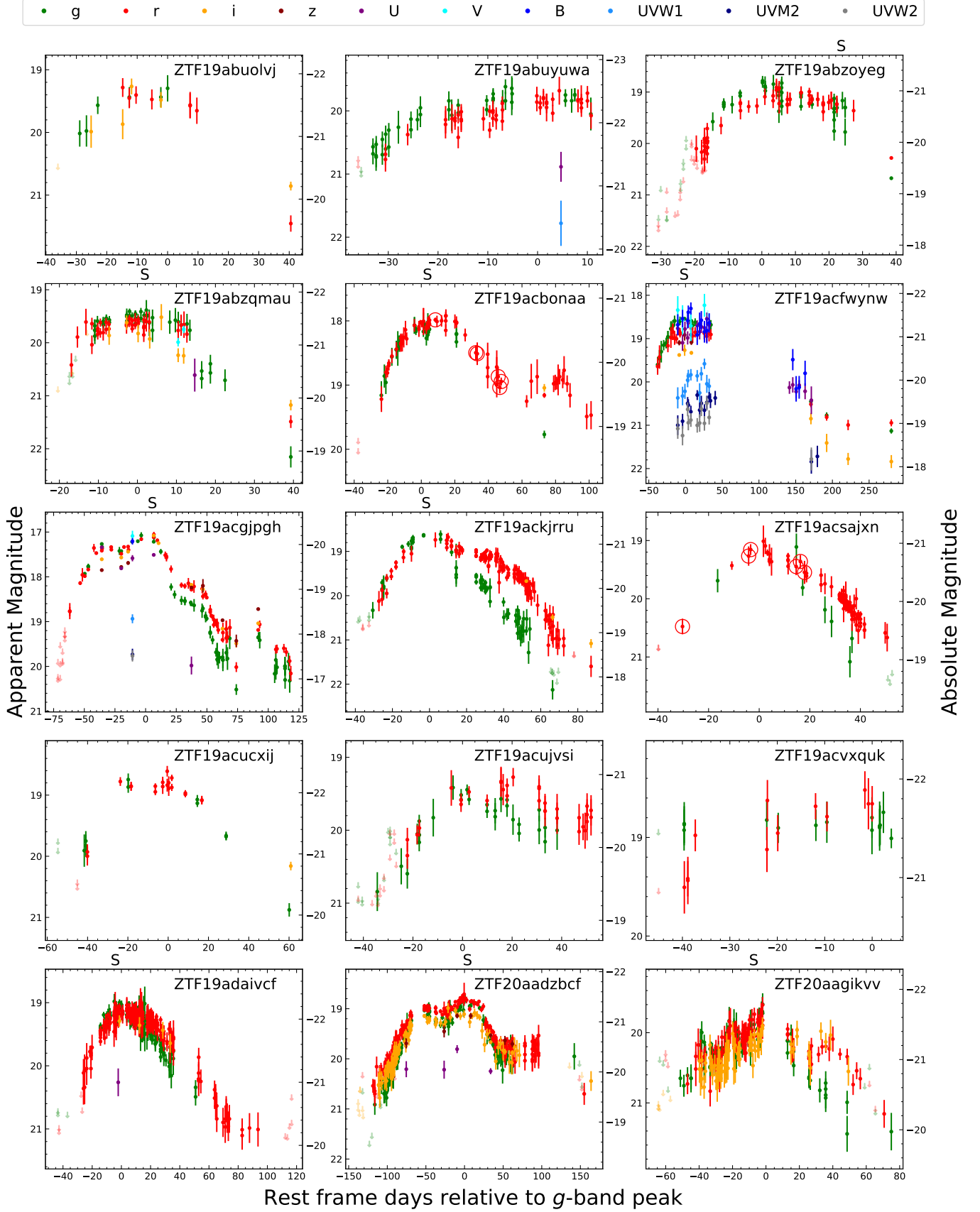


Figure A4. Similar to Figure A1.

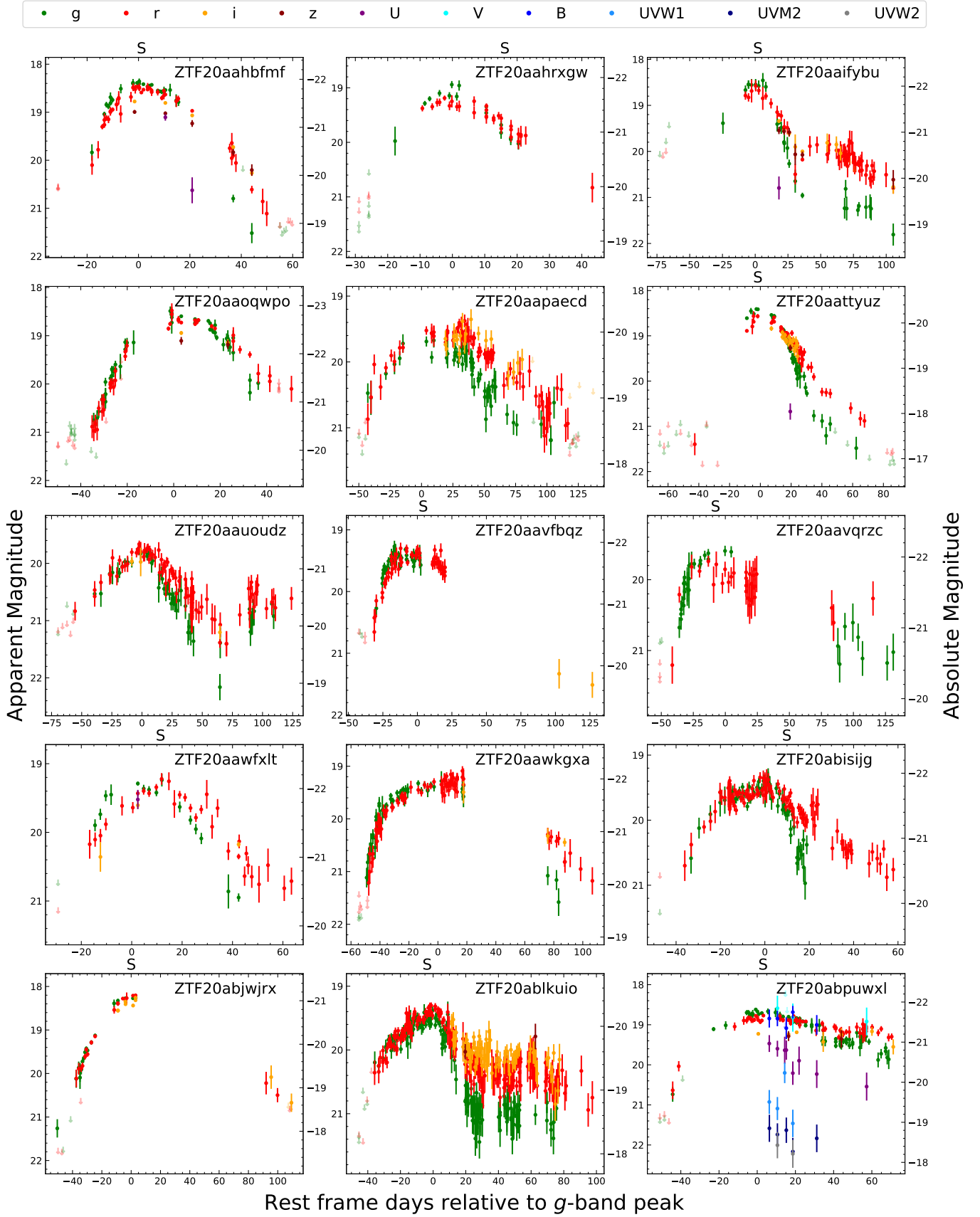


Figure A5. Similar to Figure A1.

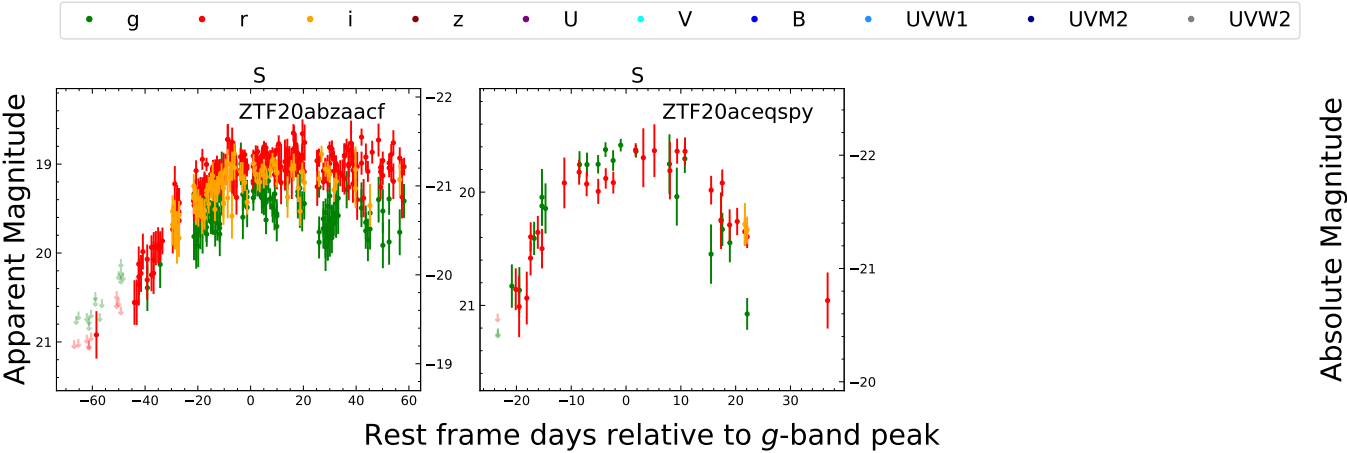


Figure A6. Similar to Figure A1.

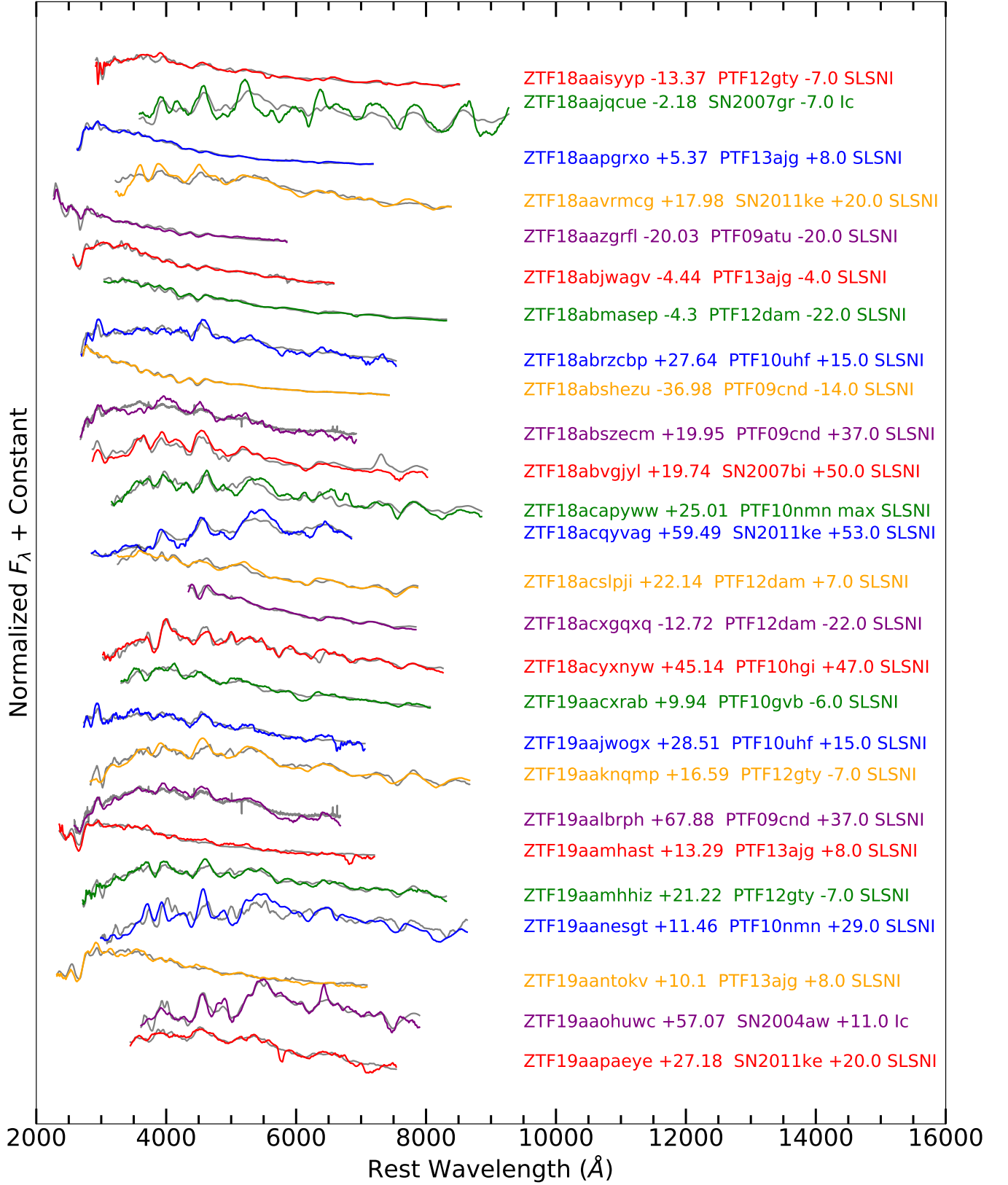


Figure A7. Spectral classification. This figure shows the comparison between our spectrum and their best-matched templates (shown in gray) from *superfit*. Event name, the phase of our spectrum (rest-frame days), the best-matched templates, the template phase and the template type are labeled after each spectrum in the same color.

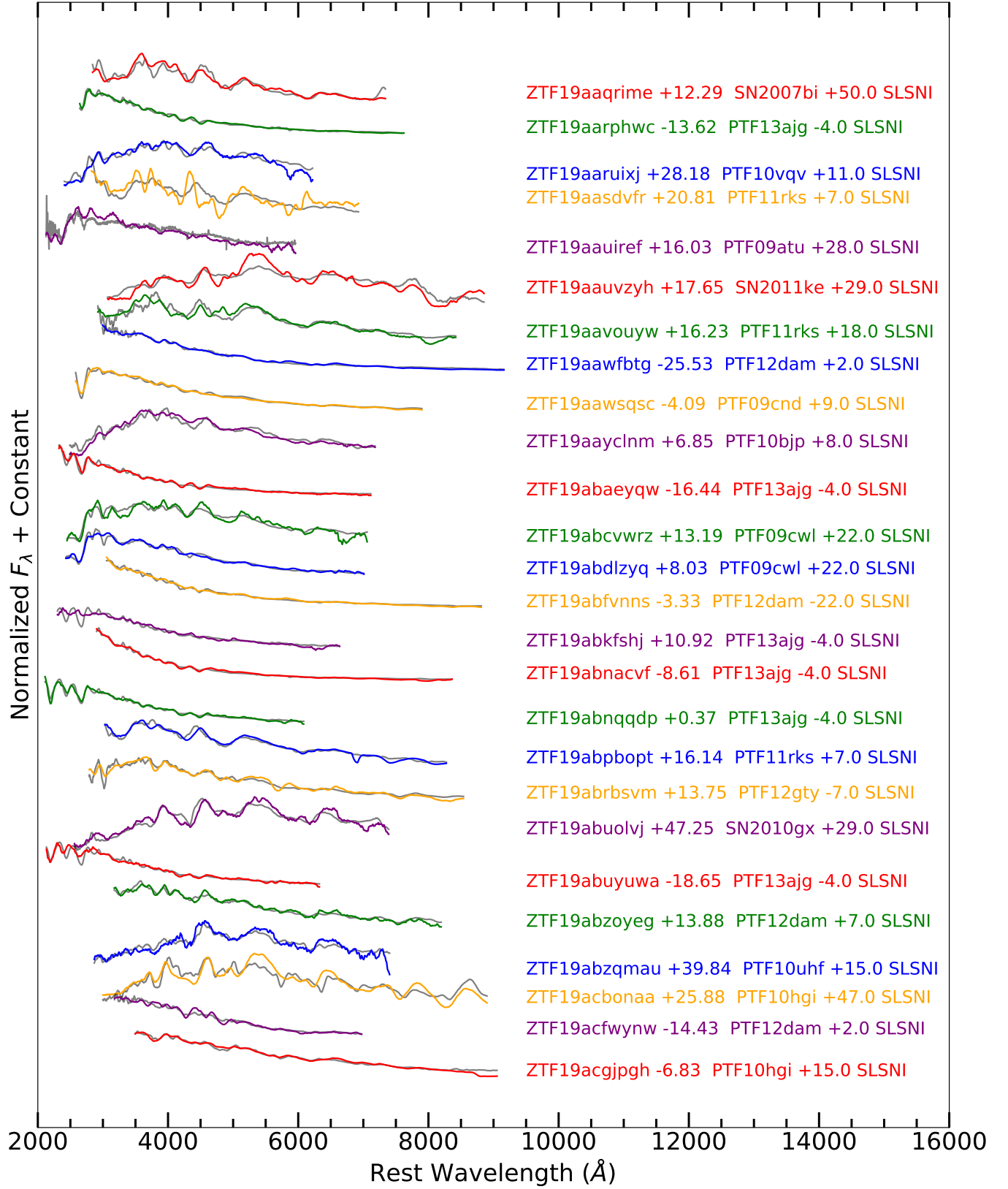


Figure A8. Similar to Figure A7

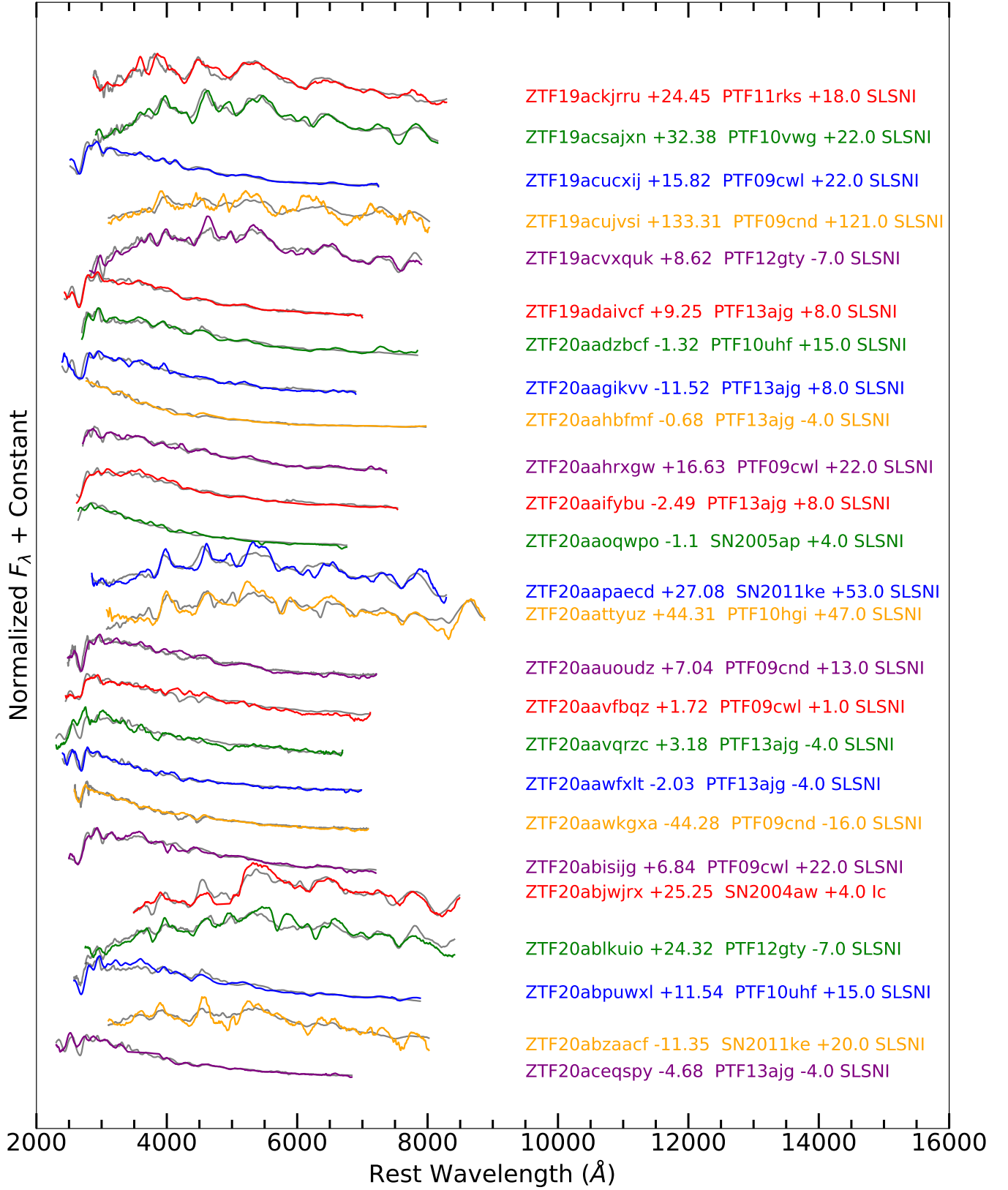


Figure A9. Similar to Figure A7

REFERENCES

- Ambikasaran, S., Foreman-Mackey, D., Greengard, L., Hogg, D. W., & O’Neil, M. 2015, *IEEE Transactions on Pattern Analysis and Machine Intelligence*, 38, 252, doi: [10.1109/TPAMI.2015.2448083](https://doi.org/10.1109/TPAMI.2015.2448083)
- Ambikasaran, S., Foreman-Mackey, D., Greengard, L., Hogg, D. W., & O’Neil, M. 2016, *IEEE Transactions on Pattern Analysis and Machine Intelligence*, 38, 252, doi: [10.1109/TPAMI.2015.2448083](https://doi.org/10.1109/TPAMI.2015.2448083)
- Anderson, J. P., Pessi, P. J., Dessart, L., et al. 2018, *ArXiv e-prints*. <https://arxiv.org/abs/1806.10609>
- Angus, C. R., Levan, A. J., Perley, D. A., et al. 2016, *MNRAS*, 458, 84, doi: [10.1093/mnras/stw063](https://doi.org/10.1093/mnras/stw063)
- Angus, C. R., Smith, M., Sullivan, M., et al. 2019, *Monthly Notices of the Royal Astronomical Society*, 487, 2215–2241, doi: [10.1093/mnras/stz1321](https://doi.org/10.1093/mnras/stz1321)
- Barbarino, C., Sollerman, J., Taddia, F., et al. 2021, *A&A*, 651, A81, doi: [10.1051/0004-6361/202038890](https://doi.org/10.1051/0004-6361/202038890)
- Bellm, E. C., Kulkarni, S. R., Graham, M. J., et al. 2019a, *PASP*, 131, 018002, doi: [10.1088/1538-3873/aaecbe](https://doi.org/10.1088/1538-3873/aaecbe)
- Bellm, E. C., Kulkarni, S. R., Barlow, T., et al. 2019b, *PASP*, 131, 068003, doi: [10.1088/1538-3873/ab0c2a](https://doi.org/10.1088/1538-3873/ab0c2a)
- Blagorodnova, N., Neill, J. D., Walters, R., et al. 2018, *PASP*, 130, 035003, doi: [10.1088/1538-3873/aaa53f](https://doi.org/10.1088/1538-3873/aaa53f)
- Blondin, S., & Tonry, J. L. 2007, *ApJ*, 666, 1024, doi: [10.1086/520494](https://doi.org/10.1086/520494)
- Chambers, K. C., Magnier, E. A., Metcalfe, N., et al. 2016, *arXiv e-prints*, arXiv:1612.05560. <https://arxiv.org/abs/1612.05560>
- Chatzopoulos, E., Wheeler, J. C., & Vinko, J. 2012, *ApJ*, 746, 121, doi: [10.1088/0004-637X/746/2/121](https://doi.org/10.1088/0004-637X/746/2/121)
- Chatzopoulos, E., Wheeler, J. C., Vinko, J., Horvath, Z. L., & Nagy, A. 2013, *ApJ*, 773, 76, doi: [10.1088/0004-637X/773/1/76](https://doi.org/10.1088/0004-637X/773/1/76)
- Chen, T.-W., Smartt, S. J., Yates, R. M., et al. 2017a, *MNRAS*, 470, 3566, doi: [10.1093/mnras/stx1428](https://doi.org/10.1093/mnras/stx1428)
- Chen, T.-W., Schady, P., Xiao, L., et al. 2017b, *ApJL*, 849, L4, doi: [10.3847/2041-8213/aa8f40](https://doi.org/10.3847/2041-8213/aa8f40)
- Chevalier, R. A., & Irwin, C. M. 2011, *ApJL*, 729, L6, doi: [10.1088/2041-8205/729/1/L6](https://doi.org/10.1088/2041-8205/729/1/L6)
- De Cia, A., Gal-Yam, A., Rubin, A., et al. 2018, *ApJ*, 860, 100, doi: [10.3847/1538-4357/aab9b6](https://doi.org/10.3847/1538-4357/aab9b6)
- Dekany, R., Smith, R. M., Riddle, R., et al. 2020, *PASP*, 132, 038001, doi: [10.1088/1538-3873/ab4ca2](https://doi.org/10.1088/1538-3873/ab4ca2)
- Dessart, L. 2019, *A&A*, 621, A141, doi: [10.1051/0004-6361/201834535](https://doi.org/10.1051/0004-6361/201834535)
- Drake, A. J., Djorgovski, S. G., Mahabal, A., et al. 2009, *ApJ*, 696, 870, doi: [10.1088/0004-637X/696/1/870](https://doi.org/10.1088/0004-637X/696/1/870)
- Drout, M. R., Chornock, R., Soderberg, A. M., et al. 2014, *ApJ*, 794, 23, doi: [10.1088/0004-637X/794/1/23](https://doi.org/10.1088/0004-637X/794/1/23)
- Duev, D. A., Mahabal, A., Masci, F. J., et al. 2019, *MNRAS*, 489, 3582, doi: [10.1093/mnras/stz2357](https://doi.org/10.1093/mnras/stz2357)
- Filippenko, A. V. 1997, *ARA&A*, 35, 309, doi: [10.1146/annurev.astro.35.1.309](https://doi.org/10.1146/annurev.astro.35.1.309)
- Fitzpatrick, E. L., & Massa, D. 2007, *The Astrophysical Journal*, 663, 320–341, doi: [10.1086/518158](https://doi.org/10.1086/518158)
- Fremling, C., Sollerman, J., Taddia, F., et al. 2016, *A&A*, 593, A68, doi: [10.1051/0004-6361/201628275](https://doi.org/10.1051/0004-6361/201628275)
- Fremling, C., Miller, A. A., Sharma, Y., et al. 2020, *ApJ*, 895, 32, doi: [10.3847/1538-4357/ab8943](https://doi.org/10.3847/1538-4357/ab8943)
- Frohmaier, C., Angus, C. R., Vincenzi, M., et al. 2021, *MNRAS*, 500, 5142, doi: [10.1093/mnras/staa3607](https://doi.org/10.1093/mnras/staa3607)
- Gal-Yam, A. 2012, *Science*, 337, 927, doi: [10.1126/science.1203601](https://doi.org/10.1126/science.1203601)
- . 2019, *ARA&A*, 57, 305, doi: [10.1146/annurev-astro-081817-051819](https://doi.org/10.1146/annurev-astro-081817-051819)
- Gal-Yam, A., Mazzali, P., Ofek, E. O., et al. 2009, *Nature*, 462, 624, doi: [10.1038/nature08579](https://doi.org/10.1038/nature08579)
- Gehrels, N., Chincarini, G., Giommi, P., et al. 2004, *ApJ*, 611, 1005, doi: [10.1086/422091](https://doi.org/10.1086/422091)
- Gezari, S., Halpern, J. P., Grupe, D., et al. 2009, *ApJ*, 690, 1313, doi: [10.1088/0004-637X/690/2/1313](https://doi.org/10.1088/0004-637X/690/2/1313)
- Graham, M. J., Kulkarni, S. R., Bellm, E. C., et al. 2019, *PASP*, 131, 078001, doi: [10.1088/1538-3873/ab006c](https://doi.org/10.1088/1538-3873/ab006c)
- Ho, A. Y. Q., Perley, D. A., Gal-Yam, A., et al. 2021, *arXiv e-prints*, arXiv:2105.08811. <https://arxiv.org/abs/2105.08811>
- Hodgkin, S. T., Harrison, D. L., Breedt, E., et al. 2021, *A&A*, 652, A76, doi: [10.1051/0004-6361/202140735](https://doi.org/10.1051/0004-6361/202140735)
- Hogg, D. W., Baldry, I. K., Blanton, M. R., & Eisenstein, D. J. 2002, *ArXiv Astrophysics e-prints*
- Howell, D. A., Sullivan, M., Nugent, P. E., et al. 2006, *Nature*, 443, 308, doi: [10.1038/nature05103](https://doi.org/10.1038/nature05103)
- Inserra, C., Prais, S., Gutierrez, C. P., et al. 2018a, *The Astrophysical Journal*, 854, 175, doi: [10.3847/1538-4357/aaaaaa](https://doi.org/10.3847/1538-4357/aaaaaa)
- Inserra, C., & Smartt, S. J. 2014, *ApJ*, 796, 87, doi: [10.1088/0004-637X/796/2/87](https://doi.org/10.1088/0004-637X/796/2/87)
- Inserra, C., Smartt, S. J., Gall, E. E. E., et al. 2018b, *Monthly Notices of the Royal Astronomical Society*, 475, 1046–1072, doi: [10.1093/mnras/stx3179](https://doi.org/10.1093/mnras/stx3179)
- Inserra, C., Sullivan, M., Angus, C. R., et al. 2021, *MNRAS*, 504, 2535, doi: [10.1093/mnras/stab978](https://doi.org/10.1093/mnras/stab978)
- Kangas, T., Blagorodnova, N., Mattila, S., et al. 2017, *MNRAS*, 469, 1246, doi: [10.1093/mnras/stx833](https://doi.org/10.1093/mnras/stx833)
- Kasen, D. 2017, *Unusual Supernovae and Alternative Power Sources*, ed. A. W. Alsabti & P. Murdin, 939, doi: [10.1007/978-3-319-21846-5_32](https://doi.org/10.1007/978-3-319-21846-5_32)

- Kasen, D., & Bildsten, L. 2010, *ApJ*, 717, 245, doi: [10.1088/0004-637X/717/1/245](https://doi.org/10.1088/0004-637X/717/1/245)
- Kasen, D., Woosley, S. E., & Heger, A. 2011, *ApJ*, 734, 102, doi: [10.1088/0004-637X/734/2/102](https://doi.org/10.1088/0004-637X/734/2/102)
- Kasliwal, M. M., Cannella, C., Bagdasaryan, A., et al. 2019, *PASP*, 131, 038003, doi: [10.1088/1538-3873/aafbc2](https://doi.org/10.1088/1538-3873/aafbc2)
- Law, N. M., Kulkarni, S. R., Dekany, R. G., et al. 2009, *PASP*, 121, 1395, doi: [10.1086/648598](https://doi.org/10.1086/648598)
- Leloudas, G., Schulze, S., Krühler, T., et al. 2015, *MNRAS*, 449, 917, doi: [10.1093/mnras/stv320](https://doi.org/10.1093/mnras/stv320)
- Lin, W. L., Wang, X. F., Li, W. X., et al. 2020, *MNRAS*, 497, 318, doi: [10.1093/mnras/staa1918](https://doi.org/10.1093/mnras/staa1918)
- Lunnan, R., Chornock, R., Berger, E., et al. 2014, *ApJ*, 787, 138, doi: [10.1088/0004-637X/787/2/138](https://doi.org/10.1088/0004-637X/787/2/138)
- . 2015, *ApJ*, 804, 90, doi: [10.1088/0004-637X/804/2/90](https://doi.org/10.1088/0004-637X/804/2/90)
- . 2018, *ApJ*, 852, 81, doi: [10.3847/1538-4357/aa9fla](https://doi.org/10.3847/1538-4357/aa9fla)
- Lunnan, R., Yan, L., Perley, D. A., et al. 2020, *ApJ*, 901, 61, doi: [10.3847/1538-4357/abaeec](https://doi.org/10.3847/1538-4357/abaeec)
- Lyman, J. D., Bersier, D., & James, P. A. 2013, *Monthly Notices of the Royal Astronomical Society*, 437, 3848–3862, doi: [10.1093/mnras/stt2187](https://doi.org/10.1093/mnras/stt2187)
- Margutti, R., Metzger, B. D., Chornock, R., et al. 2017, *ApJ*, 836, 25, doi: [10.3847/1538-4357/836/1/25](https://doi.org/10.3847/1538-4357/836/1/25)
- Masci, F. J., Laher, R. R., Rusholme, B., et al. 2019, *PASP*, 131, 018003, doi: [10.1088/1538-3873/aae8ac](https://doi.org/10.1088/1538-3873/aae8ac)
- McCrum, M., Smartt, S. J., Rest, A., et al. 2015, *MNRAS*, 448, 1206, doi: [10.1093/mnras/stv034](https://doi.org/10.1093/mnras/stv034)
- Miller, A. A., Chornock, R., Perley, D. A., et al. 2009, *ApJ*, 690, 1303, doi: [10.1088/0004-637X/690/2/1303](https://doi.org/10.1088/0004-637X/690/2/1303)
- Miller, A. A., Silverman, J. M., Butler, N. R., et al. 2010, *MNRAS*, 404, 305, doi: [10.1111/j.1365-2966.2010.16280.x](https://doi.org/10.1111/j.1365-2966.2010.16280.x)
- Nicholl, M., Guillochon, J., & Berger, E. 2017, *ArXiv e-prints*. <https://arxiv.org/abs/1706.00825>
- Nicholl, M., Smartt, S. J., Jerkstrand, A., et al. 2015, *MNRAS*, 452, 3869, doi: [10.1093/mnras/stv1522](https://doi.org/10.1093/mnras/stv1522)
- Ofek, E. O., Cameron, P. B., Kasliwal, M. M., et al. 2007, *ApJL*, 659, L13, doi: [10.1086/516749](https://doi.org/10.1086/516749)
- Oke, J. B., & Gunn, J. E. 1983, *ApJ*, 266, 713, doi: [10.1086/160817](https://doi.org/10.1086/160817)
- Oke, J. B., Cohen, J. G., Carr, M., et al. 1995, *PASP*, 107, 375, doi: [10.1086/133562](https://doi.org/10.1086/133562)
- Osterbrock, D. E., & Ferland, G. J. 2006, *Astrophysics of gaseous nebulae and active galactic nuclei*
- Pastorello, A., Smartt, S. J., Botticella, M. T., et al. 2010, *ApJL*, 724, L16, doi: [10.1088/2041-8205/724/1/L16](https://doi.org/10.1088/2041-8205/724/1/L16)
- Pedregosa, F., Varoquaux, G., Gramfort, A., et al. 2011, *Journal of Machine Learning Research*, 12, 2825
- Perley, D. A., Quimby, R. M., Yan, L., et al. 2016, *ApJ*, 830, 13, doi: [10.3847/0004-637X/830/1/13](https://doi.org/10.3847/0004-637X/830/1/13)
- Perley, D. A., Fremling, C., Sollerman, J., et al. 2020, *ApJ*, 904, 35, doi: [10.3847/1538-4357/abbd98](https://doi.org/10.3847/1538-4357/abbd98)
- Planck Collaboration, Ade, P. A. R., Aghanim, N., et al. 2016, *A&A*, 594, A13, doi: [10.1051/0004-6361/201525830](https://doi.org/10.1051/0004-6361/201525830)
- Prajs, S., Sullivan, M., Smith, M., et al. 2017, *MNRAS*, 464, 3568, doi: [10.1093/mnras/stw1942](https://doi.org/10.1093/mnras/stw1942)
- Prentice, S. J., Mazzali, P. A., Pian, E., et al. 2016, *MNRAS*, 458, 2973, doi: [10.1093/mnras/stw299](https://doi.org/10.1093/mnras/stw299)
- Quimby, R. M., Aldering, G., Wheeler, J. C., et al. 2007, *ApJL*, 668, L99, doi: [10.1086/522862](https://doi.org/10.1086/522862)
- Quimby, R. M., Yuan, F., Akerlof, C., & Wheeler, J. C. 2013, *MNRAS*, 431, 912, doi: [10.1093/mnras/stt213](https://doi.org/10.1093/mnras/stt213)
- Quimby, R. M., Kulkarni, S. R., Kasliwal, M. M., et al. 2011, *Nature*, 474, 487, doi: [10.1038/nature10095](https://doi.org/10.1038/nature10095)
- Quimby, R. M., De Cia, A., Gal-Yam, A., et al. 2018, *ApJ*, 855, 2, doi: [10.3847/1538-4357/aaac2f](https://doi.org/10.3847/1538-4357/aaac2f)
- Roming, P. W. A., Kennedy, T. E., Mason, K. O., et al. 2005, *SSRv*, 120, 95, doi: [10.1007/s11214-005-5095-4](https://doi.org/10.1007/s11214-005-5095-4)
- Schlaflly, E. F., & Finkbeiner, D. P. 2011, *The Astrophysical Journal*, 737, 103, doi: [10.1088/0004-637x/737/2/103](https://doi.org/10.1088/0004-637x/737/2/103)
- Schlegel, E. M. 1990, *MNRAS*, 244, 269
- Schulze, S., Krühler, T., Leloudas, G., et al. 2018, *MNRAS*, 473, 1258, doi: [10.1093/mnras/stx2352](https://doi.org/10.1093/mnras/stx2352)
- Shappee, B. J. 2014, PhD thesis, The Ohio State University
- Smith, N., Li, W., Foley, R. J., et al. 2007, *ApJ*, 666, 1116, doi: [10.1086/519949](https://doi.org/10.1086/519949)
- Steele, I. A., Smith, R. J., Rees, P. C., et al. 2004, in *Proc. SPIE*, Vol. 5489, *Ground-based Telescopes*, ed. J. M. Oschmann, Jr., 679–692, doi: [10.1117/12.551456](https://doi.org/10.1117/12.551456)
- Tachibana, Y., & Miller, A. A. 2018, *PASP*, 130, 128001, doi: [10.1088/1538-3873/aae3d9](https://doi.org/10.1088/1538-3873/aae3d9)
- Taddia, F., Sollerman, J., Leloudas, G., et al. 2015, *A&A*, 574, A60, doi: [10.1051/0004-6361/201423915](https://doi.org/10.1051/0004-6361/201423915)
- Taddia, F., Sollerman, J., Fremling, C., et al. 2019, *A&A*, 621, A71, doi: [10.1051/0004-6361/201834429](https://doi.org/10.1051/0004-6361/201834429)
- Taggart, K. 2020, PhD thesis, Liverpool John Moores University, doi: [10.24377/LJMU.t.00014104](https://doi.org/10.24377/LJMU.t.00014104)
- Terreran, G., Blanchard, P., DeMarchi, L., et al. 2020, *The Astronomer's Telegram*, 13970, 1
- The Dark Energy Survey Collaboration. 2005, *arXiv e-prints*, astro. <https://arxiv.org/abs/astro-ph/0510346>
- Tonry, J. L., Denneau, L., Heinze, A. N., et al. 2018, *PASP*, 130, 064505, doi: [10.1088/1538-3873/aabadf](https://doi.org/10.1088/1538-3873/aabadf)
- Wilkinson, D. M., Maraston, C., Goddard, D., Thomas, D., & Parikh, T. 2017, *MNRAS*, 472, 4297, doi: [10.1093/mnras/stx2215](https://doi.org/10.1093/mnras/stx2215)
- Woosley, S. E. 2010, *ApJL*, 719, L204, doi: [10.1088/2041-8205/719/2/L204](https://doi.org/10.1088/2041-8205/719/2/L204)
- Woosley, S. E., Blinnikov, S., & Heger, A. 2007, *Nature*, 450, 390, doi: [10.1038/nature06333](https://doi.org/10.1038/nature06333)

- Yan, L., Perley, D. A., De Cia, A., et al. 2018, ApJ, 858, 91, doi: [10.3847/1538-4357/aabad5](https://doi.org/10.3847/1538-4357/aabad5)
- Yan, L., Quimby, R., Gal-Yam, A., et al. 2017, ApJ, 840, 57, doi: [10.3847/1538-4357/aa6b02](https://doi.org/10.3847/1538-4357/aa6b02)
- Yan, L., Perley, D. A., Schulze, S., et al. 2020, ApJL, 902, L8, doi: [10.3847/2041-8213/abb8c5](https://doi.org/10.3847/2041-8213/abb8c5)
- Yao, Y., Miller, A. A., Kulkarni, S. R., et al. 2019, ApJ, 886, 152, doi: [10.3847/1538-4357/ab4cf5](https://doi.org/10.3847/1538-4357/ab4cf5)
- Yaron, O., & Gal-Yam, A. 2012, PASP, 124, 668, doi: [10.1086/666656](https://doi.org/10.1086/666656)
- Zackay, B., Ofek, E. O., & Gal-Yam, A. 2016, ApJ, 830, 27, doi: [10.3847/0004-637X/830/1/27](https://doi.org/10.3847/0004-637X/830/1/27)